To appear in The Astrophysical Journal
Preprint typeset using LaTeX style emulateapj v. 12/16/11

GAPS IN PROTOPLANETARY DISKS AS SIGNATURES OF PLANETS: II. INCLINED DISKS

Hannah Jang-Condell
Department of Physics & Astronomy, University of Wyoming, Laramie, WY 82071, U.S.A.

Neal J. Turner
Jet Propulsion Laboratory, California Institute of Technology, Pasadena, CA 91109, U.S.A. and
Max Planck Institute for Astronomy, Königstuhl 17, 69117 Heidelberg, Germany
To appear in The Astrophysical Journal

ABSTRACT

We examine the observational appearance of partial gaps being opened by planets in protoplanetary disks, considering the effects of the inclination relative to the line of sight. We model the disks with static α-models with detailed radiative transfer, parametrizing the shape and size of the partially cleared gaps based on the results of hydrodynamic simulations. As in previous work, starlight falling across the gap leads to high surface brightness contrasts. The gap's trough is darkened by both shadowing and cooling, relative to the uninterrupted disk. The gap's outer wall is brightened by direct illumination and also by heating, which puffs it up so that it intercepts more starlight. In this paper, we examine the effects of inclination on resolved images of disks with and without gaps at a wide range of wavelengths. The scattering surface's offset from the disk midplane creates a brightness asymmetry along the axis of inclination, making the disk's near side appear brighter than the far side in scattered light. Finite disk thickness also causes the projected distances of equidistant points on the disk surface to be smaller on the near side of the disk as compared to the far side. Consequently, the gap shoulder on the near side of the disk should appear brighter and closer to the star than on the far side. However, if the angular resolution of the observation is coarser than the width of the brightened gap shoulder, then the gap shoulder on the far side may appear brighter because of its larger apparent size. We present a formula to recover the scale height and inclination angle of an imaged disk using simple geometric arguments and measuring disk asymmetries. Resolved images of circumstellar disks have revealed clearings and gaps, such as the transitional disk in LkCa 15. Models created using our synthetic imaging attempting to match the morphology of observed scattered light images of LkCa 15 indicate that the H-band flux deficit in the inner $\sim 0.5''$ of the disk can be explained with a planet of mass greater than 0.5 Jupiter mass.

Keywords: planet-disk interactions – protoplanetary disks — planets: detection — radiative transfer — stars: individual (LkCa 15)

1. INTRODUCTION

An ever-increasing number of young protoplanetary disks are being imaged, from space and from the ground, and across wavelengths from optical to infrared to radio. These gas-rich disks are particularly interesting because they are the right age for giant planet formation to occur. It can be tempting to interpret structures seen in these disks as being signatures of planet formation, but without good models including radiative transfer, drawing these conclusions can be fraught. For example, scattered light images trace only the optical thin and diffuse layers of the disk and not the overall structure of the disk (Jang-Condell & Boss 2007).

This paper is the second in a series of papers analyzing gap-opening by forming planets in disks. In the first paper (Jang-Condell & Turner 2012, henceforth Paper I), we carried out detailed calculations of the vertical disk temperature and density structure in the presence of a partial gap, where the density does not approach zero in the gap. Paper I also showed simulated images of face-on disks with partial gaps in both scattered light and thermal continuum images from the optical to the radio. The utility of these models is that if a gap is well resolved so that its depth and width can be determined, then we can estimate the mass of the planet opening that gap.

Several groups have studied hydrodynamic simulations of planets opening gaps in disks in the absence of radiative heating from the central star (e.g. Paardekooper & Papaloizou 2008; Ayliffe & Bate 2009; de Val-Borro et al. 2006; Bate et al. 2003; Edgar & Quillen 2008). However, illumination on these gaps can significantly affect both the disk structure and its observable properties (e.g. Varnière et al. 2006; Turner et al. 2012, Paper I). In particular, these studies consistently find that the far edge of a gap in a flared T Tauri disk is heated and puffed up, creating a positive feedback loop that enhances the appearance of the gap.

Radiative transfer simulations on the output of hydrodynamic simulations of disks with embedded planets have been done (Jang-Condell & Boss 2007), some with particular emphasis toward predictions for ALMA (Wolf & D'Angelo 2005; Ruge et al. 2013). However, incorporating the radiative heating from stellar illumination back into the hydrodynamic simulations has thus far proven to be computationally prohibitive.

We model a gap or partial gap in the disk as a fixed perturbation on the radial surface density profile, $\Sigma(r)$

and carry out detailed radiative transfer on this disk structure, under the assumption of hydrostatic equilibrium to allow the disk to vertically expand or contract in response to heating or cooling from stellar illumination or shadowing. We assume an axisymmetric disk, so our models preclude spiral density waves. While a full three-dimensional hydrodynamic simulation including radiative transfer would be the best model for a gap in a disk, it is also very computationally intensive. The models presented here provide a useful analysis of gap opening in disks, even if some details are missing.

We make use of the radiative transfer models presented in Paper I, which exploits analytic approximations of solutions to the equations of radiative transfer to efficiently calculate disk structure. Monte Carlo methods are more accurate in a sense, since they directly track photon packets in the disk (e.g. Walker et al. 2004; Dullemond & Dominik 2004; Tannirkulam et al. 2008; Pinte et al. 2008; Mulders et al. 2010). However, their computationally intensive natures makes the iterative calculation of disk structure time consuming. The methods we adopt allow for rapid iterative calculation of disk structure in order to attain self-consistency between density and temperature in the structure of the disk. We use Monte Carlo calculations to validate selected cases.

As an example of the application of the models presented here, we consider the case of the LkCa 15 pretransitional disk. LkCa 15 is just one of a number of such transitional disks whose cavities were resolved recently, including by Hashimoto et al. (2012), Mathews et al. (2012), Cieza et al. (2012), Andrews et al. (2011b). Companion planets or low-mass stars are observed in some cases (Biller et al. 2012; Kraus & Ireland 2012; Huélamo et al. 2011).

In this paper, we examine the effects of inclination on disk images, making use of the models presented in Paper I. We show that some brightness asymmetries in disks may be purely geometrical effects, attributable to the shape of the last scattering surface and its changing appearance with inclination angle rather than anisotropic scattering. We show that these effects may be seen in disks both with and without partially cleared gaps in them. Finally, we apply our approach to images of the disk surrounding LkCa 15, to constrain the mass of the planet capable of opening the gap observed at near-infrared and millimeter wavelengths.

2. MODEL

The model for the disk structure and observable properties is the JC model presented in detail in Paper I. The disk structure model calculates radiative transfer based on the methods of Jang-Condell & Sasselov (2003) and Jang-Condell & Sasselov (2004) and adapted to iteratively calculate the temperature and density structure in a self-consistent manner as described in Jang-Condell (2008). The observable properties are calculated following Jang-Condell (2009) with modifications to approximate the effects of multiple scattering as described in Paper I.

Here, we summarize the JC model for calculating disk temperature structure and synthetic images. The JC method is a fully three-dimensional radiative transfer calculation, allowing the propagation of radiation from the disk surface to all points within the disk, both vertically and radially. It relies on a one-dimensional approximate solution for the equations of radiative transfer to calculate the propagation of photons from a given point to another, but does not otherwise assume a plane-parallel disk.

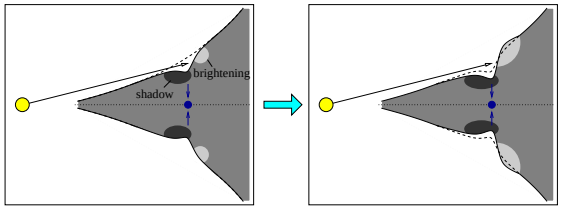

Figure 1. Cartoon diagram of radiative feedback on disk structure. The star is represented as a yellow disk, and the planet by a blue dot. The disk surface represents a contour of roughly constant density. The left image shows the initial gap opened in the disk, with the dotted line showing the original, unperturbed disk surface. Stellar illumination on the surface of the gap creates shadowed and brightened regions. Shadowing and cooling occurs in the disk trough, and the far side of the gap is illuminated and heated. The right image shows the response of the gaseous disk material to the cooling and heating: the shadowed region contracts and deepens the gap, while the illuminated far side expands and is elevated.

The only difference between the model disks in this work and Paper I is a minor modification to the opacities. The algorithm for calculating the thermal structure of the disk makes use of mean opacities. However, the mean opacities used in Paper I were inconsistent with the wavelength-dependent opacities used to calculate observables. In this work, we have rectified this inconsistency by using the correct mean opacities and recalculating the disk structure model. The opacities are an input parameter to the JC code, so the algorithms for calculating the model disk are unchanged, although the specific disk structure is modified from that presented in Paper I. We discuss this correction to the opacities is in detail in §2.1.

Gap opening is modeled as a Gaussian-shaped ad hoc perturbation to the surface density profile. We consider partially cleared gaps, where the density does not go all the way to zero within the gap. The disk temperature is then iteratively recalculated to account for the thermal adjustment of the disk to shadowing in the gap and illumination on the exposed far gap wall (see Figure 1).

Radiative heating of the disk is integrated piecewise over the surface of the disk, allowing for three-dimensional propagation of radiation throughout the disk. The parameters used to model the fiducial disk are listed in Table 1. The stellar parameters are mass $M_* = 1\,M_\odot$, radius $R_* = 2.6\,R_\odot$, and effective temperature $T_{\rm eff} = 4280$ K, consistent with a protostar with an age of 1 Myr (Siess et al. 2000). The luminosity of a star with these parameters is $L_* = 4\sigma_B \pi R_*^2 T_{\rm eff}^4 = 2.04 L_\odot$, where σ_B is the Stefan-Boltzmann constant. We assume a constant-α disk model where the viscosity is parameterized as $\nu = \alpha_{\rm ss} c_s H$ (Shakura & Sunyaev 1973), where $c_s(r)$ is the sound speed at the midplane, and $H(r)$ is the thermal scale height of the disk at radius r from the star. The disk parameters are accretion rate $\dot{M} = 10^{-8}\,M_\odot\,{\rm yr}^{-1}$ and viscosity parameter $\alpha_{\rm ss} = 0.01$, parameters typical for T Tauri stars.

2.1. *Opacities*

The mean opacities, consistent with the wavelength-dependent opacities used for calculating observables, are as follows: the Rosseland mean opacity of the disk is

Table 1
Stellar and disk parameters used for disk models

parameter	fiducial disk	LkCa 15
M_* ($M_\odot$)	1	1
R_* ($R_\odot$)	2.6	1.51
$T_{\rm eff}$ (K)	4280	4350
L_* ($L_\odot$)	2.04	0.74
$\alpha_{\rm SS}$	0.01	0.0007
$\dot{M}$ ($M_\odot\,{\rm yr}^{-1}$)	10^{-8}	2.4×10^{-9}

$\chi_R = 2.72$ cm g^{-2}, the disk temperature averaged absorption is $\kappa_P = 1.45$ cm g^{-2}, and the mean absorption and extinction averaged over the stellar spectrum are $\kappa_P^* = 1.33$ cm g^{-2} and $\chi_P^* = 10.88$ cm g^{-2}, respectively. In Paper I, the opacities adopted were $\chi_R = 2.61, \kappa_P = 1.35, \kappa_P^* = 1.61$, and $\chi_P^* = 11.75$ cm g^{-2}. The incorrect mean opacities resulted in temperatures at or above the disk surface to be too high compared to the Monte Carlo (MC) models, as shown in Figure 2. The effect on the surface temperature can be explained as follows. As described in (Jang-Condell 2008), the temperature can be approximated as

$$\frac{\sigma_B T_r^4}{\pi} = \frac{\kappa_P^*}{\chi_P^*}\frac{F_{\rm irr}\mu}{4\pi}\left[c_1 + c_2 e^{-\tau_s} + c_3 e^{-g\mu\tau_s}\right], \quad (1)$$

where $\mu(r)$ is the cosine of the angle of incidence of stellar irradiation at the surface of the disk, $F_{\rm irr}(r)$ is the stellar flux at radius r, $g = \sqrt{3(1-\omega)}$, and τ_s is the optical depth to the star. The coefficients are

$$c_1 = \frac{6 + 9\mu\chi_R/\chi_P^*}{g^2} - \frac{6(1-\chi_R/\chi_P^*)\left(3-g^2\right)}{g^2(3+2g)(1+g\mu)} \quad (2)$$

$$c_2 = \left(\frac{\chi_P^*}{\mu\kappa_P} - \frac{3\mu\chi_R}{\chi_P^*}\right)\frac{(1-3\mu^2)}{(1-g^2\mu^2)} \quad (3)$$

$$c_3 = \left(\frac{g\chi_P^*}{\kappa_P} - \frac{3\chi_R}{\chi_P^* g}\right)\frac{(2+3\mu)(3-g^2)}{g(3+2g)(1-g^2\mu^2)}. \quad (4)$$

Above the surface, $\tau \to 0$ and $\mu \to 0$. Then, to leading order in μ, $c_1 + c_2 + c_3 \to \chi_P^*/\mu\kappa_P$ and

$$T_r^4 = \frac{\kappa_P^*}{\kappa_P}\frac{F_{\rm irr}}{4\sigma_B} \quad (5)$$

The ratio κ_P^*/κ_P is decreased from 1.20 to 0.92, resulting in a temperature decrease at low optical depths of about 6%, which is the temperature decrease observed between Paper I and the fiducial disk model in this work at a radius of 10 AU and height 2.5 AU, shown in Figure 2.

Although the temperature difference is $\sim 10-20$ degrees, the alteration to the temperature occurs in the upper layers of the disk, several times the thermal scale height of the disk, which is $H = 0.48$ AU at $r = 10$ AU. The density of the disk is quite low at these heights. On the other hand, the temperature at the midplane, the densest region, is largely unchanged. Thus, the overall structure of the disk changes only slightly between Paper I and this work.

2.2. *Disk Structure*

As described in Paper I and references therein, the density and temperature structure of the disk models are calculated iteratively, keeping the total vertically-integrated surface density fixed. We refer to the disk without a gap as the fiducial model. Disks with gaps are calculated in the same way as the fiducial model, the difference being in the surface density profile used. The heating of the disk from stellar irradiation is calculated by piecewise integration over the disk surface. The density profile of the disk is then recalculated under the assumption of hydrostatic equilibrium. This process is iterated until the disk structure converges. We assume azimuthal symmetry for disk models both with and without gaps, but accounting for the three-dimensional curvature of the disk. The surface density of the gapless disk is given as Σ_0, and a disk with a gap as Σ without a subscript.

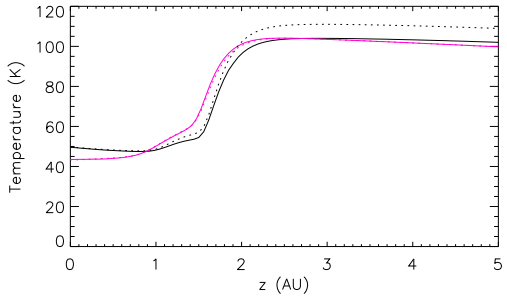

Figure 2. Vertical temperature profile of the unperturbed disk at 10 AU. JC model calculations are shown in black, and Monte Carlo comparison models are shown in magenta. Dotted lines show results from Paper I, and solid lines are this work. Incorrect mean opacities were implemented in the JC models in Paper I, yielding disk surface temperatures that were too high. Using the correct opacities, the solid black and magenta lines are nearly coincident above 2 AU.

2.3. *Gap Opening*

Gap opening by planets is modeled as an ad hoc modification to the surface density profile so that the surface density of a disk modified by a gap of width w, depth d, and position a is

$$\Sigma(r) = \Sigma_0(r)\left\{1 - d\exp[-(r-a)^2/(2w^2)]\right\}. \quad (6)$$

The values of d and w versus planet mass are determined from the results of Bate et al. (2003), using the gap-opening criterion of Crida et al. (2006),

$$G \equiv \frac{3}{4}\frac{H}{r_{\rm Hill}} + \frac{50}{q\mathcal{R}} \lesssim 1 \quad (7)$$

where we have defined G to be the gap-opening parameter, $r_{\rm Hill}$ is the Hill radius, q is the ratio of planet to stellar mass, and the Reynolds number is $\mathcal{R} \equiv r^2\Omega_P/\nu$. In the models analyzed in this paper, a 70 (200) $M_\oplus$ planet at 10 AU opens a gap of $d = 0.56(0.84)$ and width $w = 1.1(1.7)$ AU, as listed in Table 2. The shapes of the gaps are illustrated in Figure 3. We refer the gaps created by planets with $G < 1$ to be *partial* gaps because the density does not go to zero or nearly zero within the gap.

Stellar illumination on the the gap creates a shadow in the gap trough and increased illumination on the exposed far gap wall. The shadowed trough cools and contracts while the far gap shoulder heats and expands, changing the vertical density structure of the gap, as illustrated in Figure 1. The density and temperature structure of the gapped disks are iteratively recalculated to account

Table 2
Best-fit parameters for gaps opened by planets.

mass ratio[1] (q)	3×10^{-5}	1×10^{-4}	3×10^{-4}	1×10^{-3}
d	0.014	0.56	0.84	0.99
w/a	0.078	0.11	0.17	—[2]
gap-opening parameter (G)	18.4	6.2	2.5	1.04
Fiducial Disk Model (planet at 10 AU, $H/a = 0.048$)				
derived q	6.7×10^{-5}	2.2×10^{-4}	6.2×10^{-4}	1.9×10^{-3}
derived planet mass[3]	22 $M_\oplus$	72 $M_\oplus$	210 $M_\oplus$	620 $M_\oplus$
LkCa 15 Model				
planet position[4] (a)	···	40.7 AU	38.3 AU	32.5 AU
disk aspect ratio[5] (H/a)	···	0.0609	0.0600	0.0569
derived q	···	3.1×10^{-5}	1.08×10^{-4}	4.6×10^{-4}
derived planet mass	···	10.6 $M_\oplus$	37.3 $M_\oplus$	154 $M_\oplus$

[1] As simulated in Bate et al. (2003)
[2] The gap opened by the $q = 10^{-3}$ planet in the Bate et al. (2003) simulation is not well-modeled by a Gaussian.
[3] Actual masses used for this work. In the text, the masses have been rounded to 20, 70, and 200 $M_\oplus$ for convenience.
[4] Determined by wall creation at 46 AU
[5] Calculated from disk properties at planet position

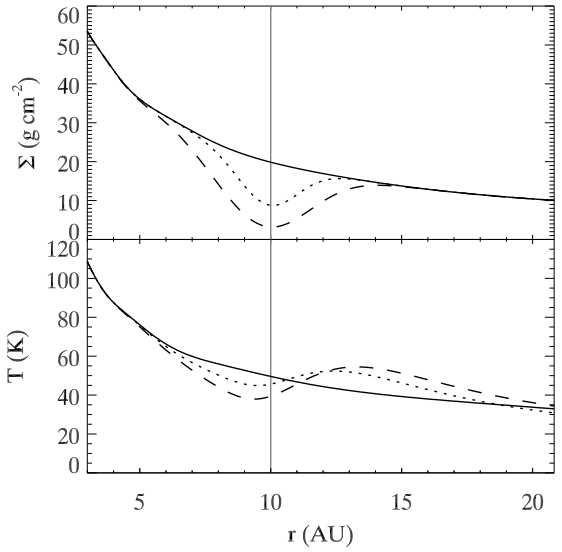

Figure 3. Surface density (top) and midplane temperature (bottom) profiles for a disk with and without a gap created by a planet at 10 AU. Solid, dotted, and dashed lines indicate planet masses of 0, 70, and 200 $M_\oplus$, respectively. The thermal perturbation is caused by shadowing and illumination by stellar irradiation at the disk surface.

for these changes. The resulting midplane temperature profiles are plotted in Figure 3.

2.4. *Observables*

We consider two main modes of disk emission: scattered stellar light and thermal emission from the disk. Full details of the calculations are described in Paper I, but we summarize the essential model below.

Scattered light contributions are calculated using local conditions in the surface of the disk and the geometry of the scattering angles. The scattering surface is determined to be where the optical depth to light from the star at frequency ν is $\tau_{\nu,*} = 2/3$. In the case of single isotropic scattering, the brightness of scattered light from a given point on the scattering surface is

$$I_1^s(\nu) = \frac{\omega_\nu \mu R_*^2 B_\nu(T_*)}{4r^2(\mu + \cos\eta)}, \tag{8}$$

where μ is the cosine of the angle of incidence of stellar light on the surface, ω_ν is the wavelength-dependent albedo, r is the distance between the surface and the star, η is the viewing angle, defined as the angle of scattering to the observer with respect to the surface normal, and $B_\nu(T_*)$ is the stellar brightness at ν, evaluated as the Planck function.

The contribution to disk brightness from photons scattered two or more times is

$$I_2^s = \frac{B_\nu(T_*)R_*^2}{4r^2}\frac{\mu\omega^2}{1-g^2\mu^2} \times \left[\frac{2+3\mu}{(1+2g/3)}\frac{1}{(1+g\cos\eta)} - \frac{3\mu}{(1+\cos\eta/\mu)}\right] \tag{9}$$

where $g = \sqrt{3(1-\omega_\nu)}$ and isotropy is assumed. Then the total brightness from scattered light is

$$I_\nu^s = I_1^s + I_2^s = \frac{\omega_\nu \mu R_*^2 B_\nu(T_*)}{4r^2(\mu+\cos\eta)} \times \left\{1 + \frac{\omega_\nu}{1-g^2\mu^2}\left[\frac{(2+3\mu)(\mu+\cos\eta)}{(1+2g/3)(1+g\cos\eta)} - 3\mu^2\right]\right\} \tag{10}$$

Note that the viewing angle η is distinct from the inclination angle i, as i is a global value assigned to a disk referring to the tilt of the disk midplane with respect to the observer, whereas η is a local value within the disk, and depends on both i and the local disk shape. The angles are illustrated in Figure 4, which shows that for larger values of η ($\eta_2 > \eta_1$), the observer sees more scatterers along the line of sight, resulting in an apparent brightening of the surface layer.

The thermal emission is calculated as in Paper 1 to include multiple scattering of thermally emitted photons

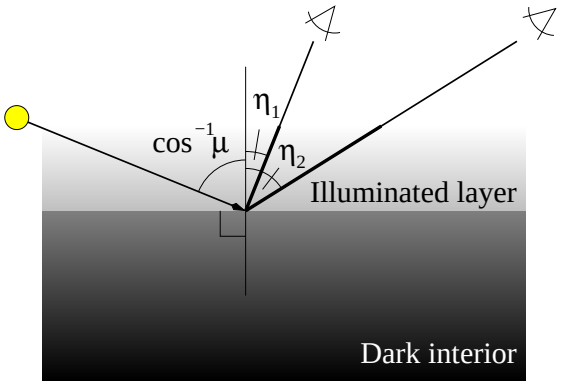

Figure 4. Illustration of how inclination affects brightness of scattered light. The path length through the illuminated layer represents the relative brightness seen by each observer. The cosine of the angle of incidence of stellar light at the surface is μ. The angle between the surface normal and the observer is η. For $\eta_2 > \eta_1$, there are more scatterers along the path through the illuminated layer for the observer at η_2, so the disk appears brighter.

within the disk. The source function is given by

$$S_\nu = \omega_\nu J_\nu + (1-\omega_\nu) B_\nu \tag{11}$$

where ω_ν is the wavelength-dependent albedo, $B_\nu = B_\nu(T)$ is the local thermal emission, and J_ν is the mean intensity. The mean intensity, assuming local thermodynamic equilibrium, is given by

$$J_\nu = B_\nu(T)\left[1 - \frac{\exp\left[g(\tau_\nu - \tau_{\max})\right] + \exp\left(-g\tau_\nu\right)}{\left(1 - g/\sqrt{3}\right)\exp\left(-g\tau_{\max}\right) + 1 + g/\sqrt{3}}\right], \tag{12}$$

where $\tau_\nu/\cos i$ is the optical depth at frequency ν integrated along the line of sight and $\tau_{\max}$ is the maximum value of τ_ν when integrated all the way through the disk. The emitted intensity I^t_ν is found by integrating the equation of radiative transfer for a locally plane-parallel medium,

$$\cos\eta \frac{\partial I^t_\nu}{\partial \tau_\nu} = I^t_\nu - \omega_\nu J_\nu - (1-\omega_\nu) B_\nu \tag{13}$$

with the assumption that the disk is geometrically thin ($\eta \approx i$). The mean intensity is evaluated along the line of sight through the disk, and τ_ν is measured as the optical depth perpendicular to the disk.

A disk image is assembled pixel by pixel. Each pixel represents a particular line of sight through the disk. For scattered light images, we find where the line of sight intercepts the disk surface, and calculate r, μ and η at that point to obtain the disk brightness from Equation (10). For thermal emission, Equation (13) is integrated along the line of sight represented by each pixel.

3. RESULTS

Using the methods outlined in §2 and detailed in Paper I, we calculate the thermal structure of a protoplanetary disk with and without gaps created by planets. We choose two gap sizes, corresponding the planet masses of 70 and 200 $M_\oplus$. These models are the same as those presented in Paper I, with a correction to the opacities that produces only a minor modification to the disk structure in the low density upper layers. We then simulate images of these disks at a range of wavelengths $(1, 10, 30, 100, 300,$ and $1000\,\mu$m), and varying inclination angle ($0°, 30°, 45°$, and $60°$.

3.1. *Validation*

As in Paper I, we compare the resulting disk models to Monte-Carlo (MC) models (Turner et al. 2012). Where not otherwise specified, our MC runs use 10^9 photons each. The final two-dimensional density structure (assuming azimuthal symmetry) of each disk model is fed into the MC code to produce a comparison temperature model of the disk, and accompanying observables.

In Paper I, we demonstrated that the JC and MC models give qualitatively consistent results for the thermal structure of the disk. One inconsistency was that the temperatures above the disk surface were hotter in the JC models than the MC models. This was a result of incorrect mean opacities used as input parameters, and this has been corrected in the present work and explained in detail in §2.1. The JC models presented here are otherwise calculated in exactly the same way as in Paper I. Since the temperatures affected were in the upper, least dense layers of the disk, the effect of this correction on the overall disk structure was minor, and the results of Paper I are not significantly affected.

In Figure 5, we show the temperature cross-sections as contour plots resulting from the JC (a,c,e) and MC (b,d,e) models. Figures 5c–5f show the cooling and heating created by shadowing and illumination on gaps in the disk, as ΔT. The apparent heating at the disk surface seen at 10 AU and inward is caused by the cooling and contraction of the disk, which lowers the disk surface. Since the disk surface is hotter than the interior, the region of space now above the photosphere is hotter that it was in the unperturbed disk case.

As noted in Paper I, the temperature structure of the disk is qualitatively similar in both the JC and MC radiative transfer models. However, there were a few notable deviations. First, the temperature of the surface was ∼10 K hotter in the JC model. This has been corrected by implementing the correct values for the mean opacities, as illustrated in Figure 2. As the temperature corrections occur mostly in the upper layers of the disk, where the density is low, the change to the structure of the disk is small. Thus, the results presented in Paper I are qualitatively still relevant.

Second, the midplane temperatures are $\sim 10K$ hotter in the JC model. This is likely a result of the fact that the analytical solution used to estimate heating contributions from individual surface elements to points within the disk assumes a semi-infinite slab. This would result in overheating at high optical depths, since in a finite-thickness medium, photons could escape out the other side of the slab.

Third, the depth of surface heating is deeper in the MC model, so that the photosphere is generally hotter. This is likely because the use of mean opacities in the JC model means that all photons are treated as having the same opacity, while the MC model implements wavelength-dependent opacities, allowing photons longward of the stellar blackbody peak but still shortward of the disk thermal peak to penetrate deeper into the disk and heat those regions. This explains the additional cooling seen in the JC model in Figure 5e just inside 10 AU, as well as the closer spacing of temperature contours

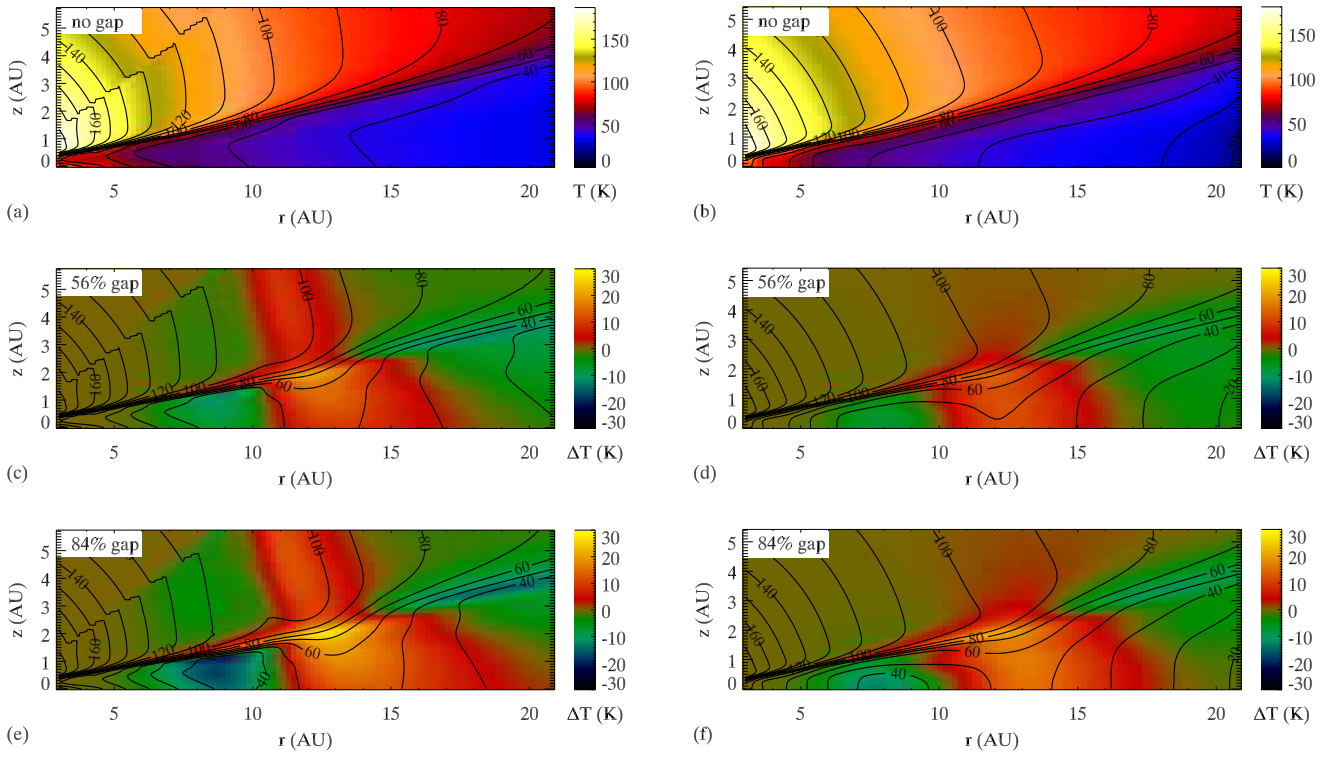

Figure 5. Temperature cross-sections of model disks, where r is the radial distance and z is vertical height above the midplane. The JC model is shown in subfigures (a), (c), and (e), while the MC model is shown in (b), (d), and (f). The height axis is scaled to the radial axis, so the aspect ratio is correct. Contours indicate temperature in Kelvins and are spaced at 10K intervals. (a,b): The temperature profile of a disk without a planet or gap. The color scale shows the temperature. (c-f): The temperature profiles of disks with gaps at 10 AU from the star, and created by a 70 $M_\oplus$ (c,d) and 200 $M_\oplus$ planet (e,f). Contours show the absolute temperature, and the color scale shows the temperature difference (ΔT) as compared to that in the unperturbed gap-less disk, with green to blue colors showing regions that have cooled and red to yellow colors showing regions that have heated.

near the disk surface in the JC model. Correcting this would involve abandoning the analytic solution to the radiative transfer equation that enables the speed of the computation, but this is outside the scope of the current paper.

Fourth, the JC models show a greater degree of heating than the MC models above the surface at radii just above the radial position of the gap, as shown by the red regions in Figures 5c and 5e at around $r = 12$ AU and $z \gtrsim 2$ AU. This is due to the interpolation of temperatures above and below the surface in the JC model. In constrast, the MC models show little change in temperature above the disk surface, as shown in Figures 5d and 5f. As this region above the disk surface is diffuse and contributes little to the disk structure or to observations, the difference in temperatures does not significantly affect either the interior of the disk or any observables. Thus, we set aside the resolution to this problem for future work.

As discussed in Paper I, despite the differences in the temperature structures of the JC and MC models, they give good qualitative agreement. Examining Figures 5c-f, both models show that when a partial gap is opened in a disk, material is cooled in the gap trough (the green areas around $r = 10$ AU) while the far wall is heated (the red to yellow regions outward of 10 AU). The models also agree that the heated and puffed up outer gap wall should shadow the regions still further outward (green areas roughly around $r > 15$ AU and $z \sim 30$ AU). This effect was also seen in models of solar illumination on the gap opened by Jupiter (Turner et al. 2012), which used the same radiative transfer modeling as the MC models.

We calculate 1 μm scattered light model images of our disks with both the JC and MC models with an inclination of 45°, and compare our results in Figure 6. Overall, there is good agreement in the morphology of both sets of disk models. The brightness of the far gap wall is similar in magnitude, and the shape of the bright ring is nearly identical.

The differences in the two sets of models are the same model differences seen in Paper I, for face-on disks. As seen in Paper I, the JC models predicts a deeper shadow in the gap trough than the MC model. This is likely because while the JC model treats multiple scattering locally, it does not consider photons scattered into the gap from the brightened far gap wall, which may brighten the gap trough.

The MC model also predicts a brighter inner disk, especially close to the star. This may be a result of a different treatment of the inner boundary condition. The JC code assumes an analytic profile for the inner disk, while the MC calculations treat no transfer there, simply discarding each photon arriving directly from the star that would be absorbed or scattered in the innermost modeled annulus.

Although there are some differences between the simulated images of the disks, qualitatively they show the same features: darkening in the gap trough and bright-

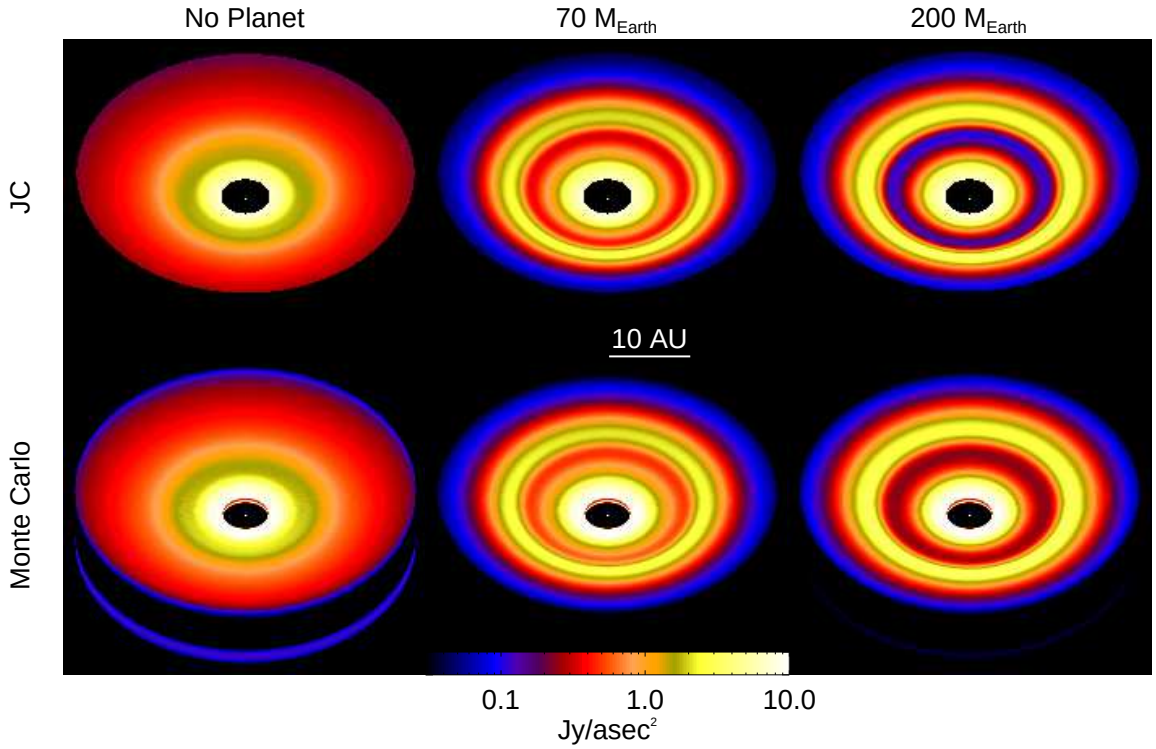

Figure 6. Comparison of scattered light images using JC models (top) and a Monte Carlo code (MC, bottom). The disks are tilted at 45° and the images are calculated at 1 micron. The left panels show disks with no gaps. The center/right panels show disks with gaps opened by a 70/200 $M_\oplus$ planet. JC models and MC models give similar results, validating our use of the JC models henceforth.

ening on the far gap shoulder. Moreover, the morphology of the images of tilted gaps is nearly identical. In both the JC and MC models, the near side of the disk (bottom half of each image) appears forshortened in comparison to the far side. This is evidenced by the narrowing of both the gap shadow and the brightened outer shoulder on the near side of the images. Moreover, the near side of the disk is slightly brighter than the far side of the disk in both the MC and JC models. The reasons for these effects are described in the remainder of this section.

3.2. *Simulated Images of Inclined Disks*

Henceforth, unless specifically referred to otherwise, the disk models discussed are the JC models. We are interested in the effect of the appearance of disks with and without gaps as the inclination angle varies. To aid in the interpretation of the effects of inclination on disk images, we present a schematic of disk tilted at an inclination i with respect to the observer in Figure 7, and will refer to the angles and distances defined in it throughout.

In particular, we note that an axisymmetric structure of radius r_d on the surface of the disk, when projected on the sky, will appear asymmetric along the minor axis, having a projected distance of r_n on the near side of the disk (the lower right half of the schematic disk) and r_f on the far side of the disk (upper left half). This is because of the finite thickness of the disk: if the structure was in the midplane of the disk, then $r_f = r_n$.

We also note that if the slope of the disk surface is given by $\tan\alpha$ at the position of this same hypothetical axisymmetric disk structure, then the local viewing angles, η_1 and η_2 for the far side and near side, respectively, are not equal, and are given by $\eta_1 = i - \alpha$ and $\eta_2 = i + \alpha$. This will become relevant in discussing brightness asymmetries seen in the simulated disk images.

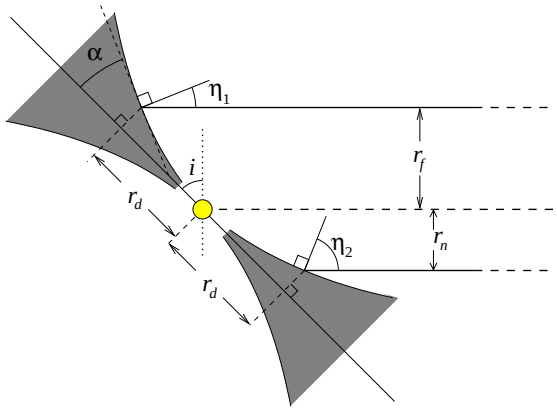

Figure 7. Schematic of inclination and aspect angles in the disk. The yellow circle represents the central star and the gray flared wedges represent the optically thick interior of the disk in cross-section. Points that are equidistant from the star in the deprojected disk with a distance of r_d appear to be at different distances on the near side versus the far side of the disk when the disk is inclined at an inclination angle of i. The observer sees only the surface of the disk above the optically thick region. The aspect angle α is the angle that this surface makes with the disk midplane. The points on the near and far sides of the disk appears to be at a distances r_n and r_f, respectively. Moreover, the viewing angles along these lines of sight are different, with $\eta_1 = i - \alpha$ and $\eta_2 = i + \alpha$. Since $\eta_2 > \eta_1$, the nearer line of sight traverses a greater path length in the bright disk atmosphere and therefore appears brighter than the far point.

3.2.1. *Inclined Disks: No Gap*

In Figures 8−13, we demonstrate the effect of inclination on the appearance disks when imaged at 1 μm to 1 mm, with and without gaps. The top row of each figure shows variously inclined disks without a gap. In each im-

age, the disk is inclined so that the top edge tilted away from the observer. First, let us consider the fiducial disk model, in the absence of any gap.

In the images at shorter wavelengths, the inclined disks appear vertically asymmetric because the emission is from the disk surface, which is essentially bowl-shaped. A schematic for the geometry is illustrated in Figure 7, which shows a cartoon schematic of a disk around a star. The lines of sight marked by the angles η_1 and η_2 intersect the disk at the same distance from the star, but because the surface is above the midplane, the projected distance on the sky is not equal, as can be seen by comparing the distance between the solid lines to the dashed line intersected in the star. This causes an apparent foreshortening of the near side of the disk. Moreover, since $\eta_2 > \eta_1$, the near side appears brighter than the far side. This is can be seen in the 1 μm images in the top row of Figure 8. The foreshortening of the near side of the disk is also evident in the 10 and 30 μm images, in Figures 9 and 10. At 0.1 mm and longer (Figures 11, 12, and 13), the optical depth decreases with increasing wavelength, so the vertical asymmetry diminishes. The apparent thick rim on the disk's near side results from truncating the calculation at 21 AU and should be ignored.

The surface brightness profile at 1 μm along the major axis of the tilted disk is systematically brighter as compared to the face on disk, as seen in the upper left plot of Figure 14. The amount of brightening increases with increasing inclination angle. However, this is not reproduced at wavelengths longward of 30 μm. This can be explained as follows. At 1 μm, the disk image is purely scattered light. Thus, Equation (10) governs the brightness profile. Assuming $\mu \ll 1$, which is generally the case, then the brightness depends on the viewing angle η as $\sim 1/\cos\eta$. While Eq. (10) is derived in detail in Paper I, another representation for the scattered light brightness is illustrated in Figure 4. In essence, the star illuminates an optically thin layer of scatterers on the surface of the disk. For $\mu \ll 1$, the brightness is roughly proportional to the number of scatterers along the line of sight, which is in turn proportional to $1/\cos\eta$. When the disk is inclined at angle i, $\cos\eta = \cos\alpha\cos i$, along the major axis (at maximum elongation), as shown in Appendix A. Since α is the angle of the disk surface with respect to the disk midplane and is intrinsic to the disk itself, the brightness profile along the major axis of the inclined disk scales as $1/\cos i$ as compared to the face on disk. As i increases, $1/\cos i$ increases as well.

A similar effect occurs with the thermal emission to a limited extent. As seen in Figure 5, the surface of the disk is generally hotter than the optically thick interior. At wavelengths close to the blackbody peak of the surface temperature, an inclination effect similar to that of the scattered light will occur. Since temperature decreases with distance in the disk at both the surface and the midplane, the wavelength of observation may be tuned to probe the surface at a particular distance in the disk. At 10 AU in this disk model, the surface temperatures are above 100K while the interior is below 100K, so 30 μm imaging is a good probe of the surface of the disk. Wavelengths longer than 30 microns are sensitive to the interior of the disk both because the disk becomes optically thin and because the interior is cooler than the surface. This is illustrated in the disk profiles in Figure 14, where the cyan lines indicating the major axis of the tilted disks are all systematically brighter than the face-on disk for $\lesssim 30$ microns, whereas at longer wavelengths the major axis profiles are less than or equal to the face-on profiles.

In Table 3 we list the heights and slopes of the disk surface at 10 AU at the listed wavelength. For wavelengths dominated by scattered light, we define the imaging surface, $z_s(r)$, to be where the disk becomes optically thick to stellar light at the given wavelength. That is, $\tau_\lambda = 2/3$ as measured along the line of sight to the star. At scattered light wavelengths (1 and 10 microns), $\mu \approx \partial z_s/\partial r - z_s/r$, and typically $\mu \ll 1$. For thermal wavelengths ($\lambda \geq 30$ μm), the surface is defined to be where the optical depth to observer in a face-on orientation becomes optically thick. That is, $\tau_\lambda = 2/3$ measured perpendicular to the disk.

In addition to the brightness asymmetry, the projected distance at a given radial distance on the disk's surface is foreshortened on the near side of the disk compared to the far side. If r_n and r_f are the projected distances along the near and far sides of the disk, respectively, r_d is the actual distance, and $\tan\beta(r) = z_s(r)/r$, then

$$r_n = r_d\cos(i+\beta)/\cos\beta \quad \text{and} \tag{14}$$

$$r_f = r_d\cos(i-\beta)/\cos\beta. \tag{15}$$

Note that these relations rely on the assumption that the imaging surface of the disk is independent of viewing angle. This assumption is valid for scattered light, where the illuminated surface layer is thin compared to the depth to which the observer sees: that is, $\tau \sim 1$ to the star occurs higher above the midplane than $\tau \sim 1$ to the observer. This implies that the observer sees the entirety of the illuminated layer, although its brightness changes with viewing angle.

Using Equations (14)-(15) to rescale the radial distance, we can deproject the surface brightness profiles to bring them in line with what would be observed were the disk face-on. In Figure 14, we plot the deprojected surface brightness profiles along the far and near sides of the disk as dashed red and blue lines, respectively. In the 1 μm plot, the near side brightness profile appears brighter than the major axis, while the far side appears dimmer, as expected.

The brightness asymmetry between the near and far sides of the disk, represented by red and blue lines in Figure 14, can be quantified in terms of the disk geometry as well. Suppose the slope of the surface $\partial z_s/\partial r = \tan\alpha$ at $r = r_d$ and the disk is inclined at an angle i. Let η_1 and η_2 be the the angles between the surface normal and the observer on the far side and near side, respectively. This is illustrated in Figure 7. By geometry, $\eta_1 = i - \alpha$ and $\eta_2 = i + \alpha$. A more general formulation for η is discussed in Appendix A.

Let $F_0(r_d)$ be the surface brightness of the face-on disk at the projected distance r_d. For a tilted disk, the same three-dimensional radial distance is seen in projection at r_d, r_n, and r_f along the major axis, near side minor axis, and far side minor axis, respectively. The corresponding surface brightnesses are $F_m(r_d)$, $F_n(r_n)$, and $F_f(r_f)$. While these points are at the same physical distance from the star on the disk, they appear to be at

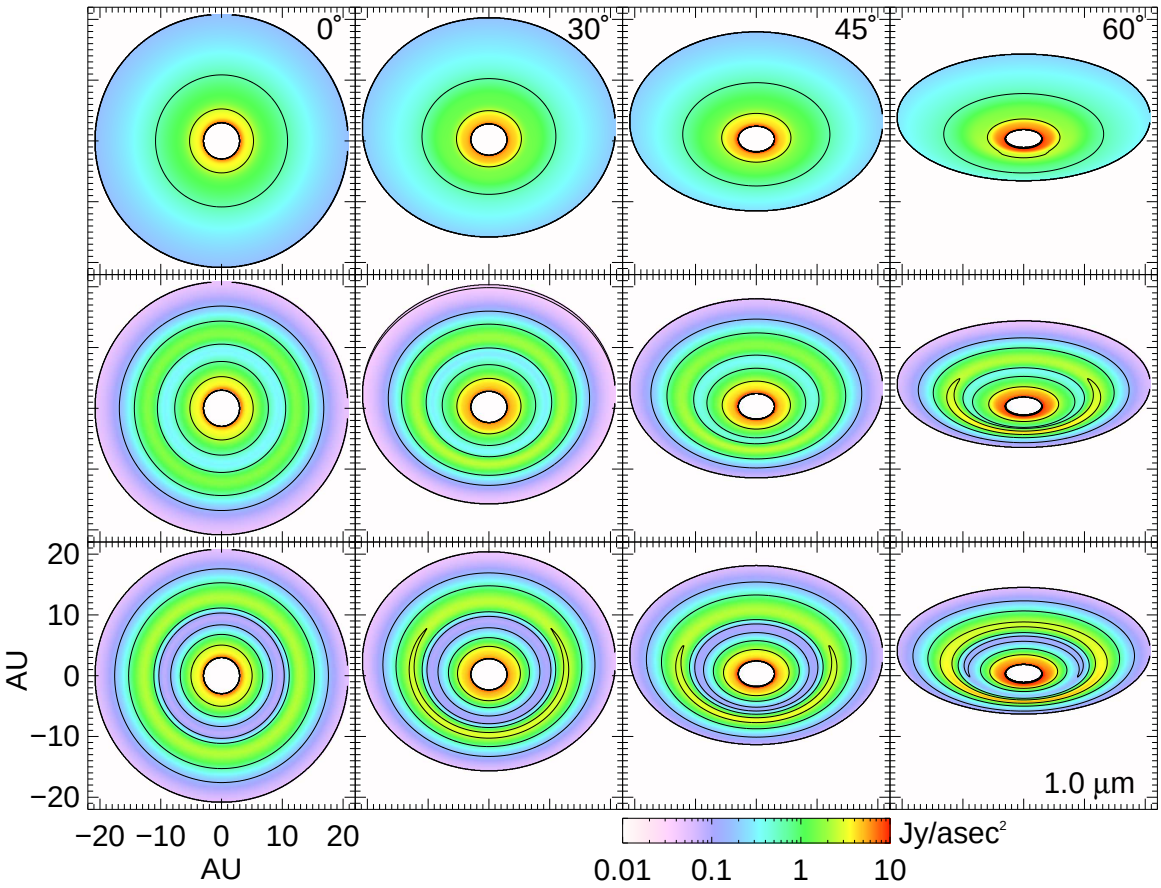

Figure 8. Images at 1 μm of disks with and without gaps viewed at various inclination angles. The top row of images show a disk without a gap. The middle (bottom) row shows images of a disk with a partial gap created by a 70 (200) $M_\oplus$ planet. From left to right, the inclination angles are 0°, 30°, 45°, and 60°. In each image, the upper part of the disk is tilted away from the observer. The scale for disk brightness is shown in the colorbar at the bottom. Contours are spaced by a factor of 4 in brightness.

Table 3
Disk inclinations calculated from simulated images.

λ (μm)	emission type	actual† $\partial z_s/\partial r$	actual† z_s/r	$i = 30°$ i	$i = 30°$ z_s/r	$i = 45°$ i	$i = 45°$ z_s/r	$i = 60°$ i	$i = 60°$ z_s/r
1	scattered	0.221	0.185	29.8°	0.185	44.6°	0.183	59.3°	0.191
10	scattered	0.200	0.170	29.7°	0.168	44.5°	0.171	59.1°	0.207
30	thermal	0.112	0.109	29.9°	0.172	44.9°	0.177	59.7°	0.177
100	thermal	0.099	0.100	30.0°	0.115	45.2°	0.104	60.1°	0.110
300	thermal	0.081	0.085	30.2°	0.047	45.4°	0.041	60.5°	0.050
1000	thermal	0.052	0.066	30.5°	0.002	45.9°	0.000	61.0°	0.003

† Measured at $r = 10$ AU

different distances when seen in projection and appear to be different brightnesses because the values of η are different in Eq. (10). In particular, $F \propto 1/(\mu + \cos\eta)$. For the face-on disk, $\eta = \alpha$. Thus, we find that the brightness profiles along the major axis, near minor axis, and far minor axis are, respectively,

$$F_m(r_d)/F_0(r_d) = (\mu + \cos\alpha)/(\mu + \cos\alpha\cos i) \quad (16)$$
$$F_n(r_n)/F_0(r_d) = (\mu + \cos\alpha)/[\mu + \cos(i + \alpha)] \quad (17)$$
$$F_f(r_f)/F_0(r_d) = (\mu + \cos\alpha)/[\mu + \cos(i - \alpha)]. \quad (18)$$

Note that these relations rely on the assumption that the imaging surface of the disk (z_s) is locally plane-parallel, since the calculations for the brightnesses as detailed in section §2.4 also rely on that assumption.

Eq. (16) is the harmonic mean of Eqs. (17) and (18), so we find the relation

$$\frac{1}{2}\left[\frac{1}{F_n(r_n)} + \frac{1}{F_f(r_f)}\right] = \frac{1}{F_m(r_d)}. \quad (19)$$

This means that given the correct values of i and β to deproject r_n and r_f according to Eqs. (14)-(15), then the harmonic mean of the deprojected surface brightness profiles on the near and far sides of the disk should equal the brightness profile along the major axis. This harmonic mean is plotted as black dashed lines in Figure 14, which does indeed prove to be a good fit to the cyan line at all wavelengths.

We can make use of this relation to construct a simple geometric model for a tilted disk image, and then apply

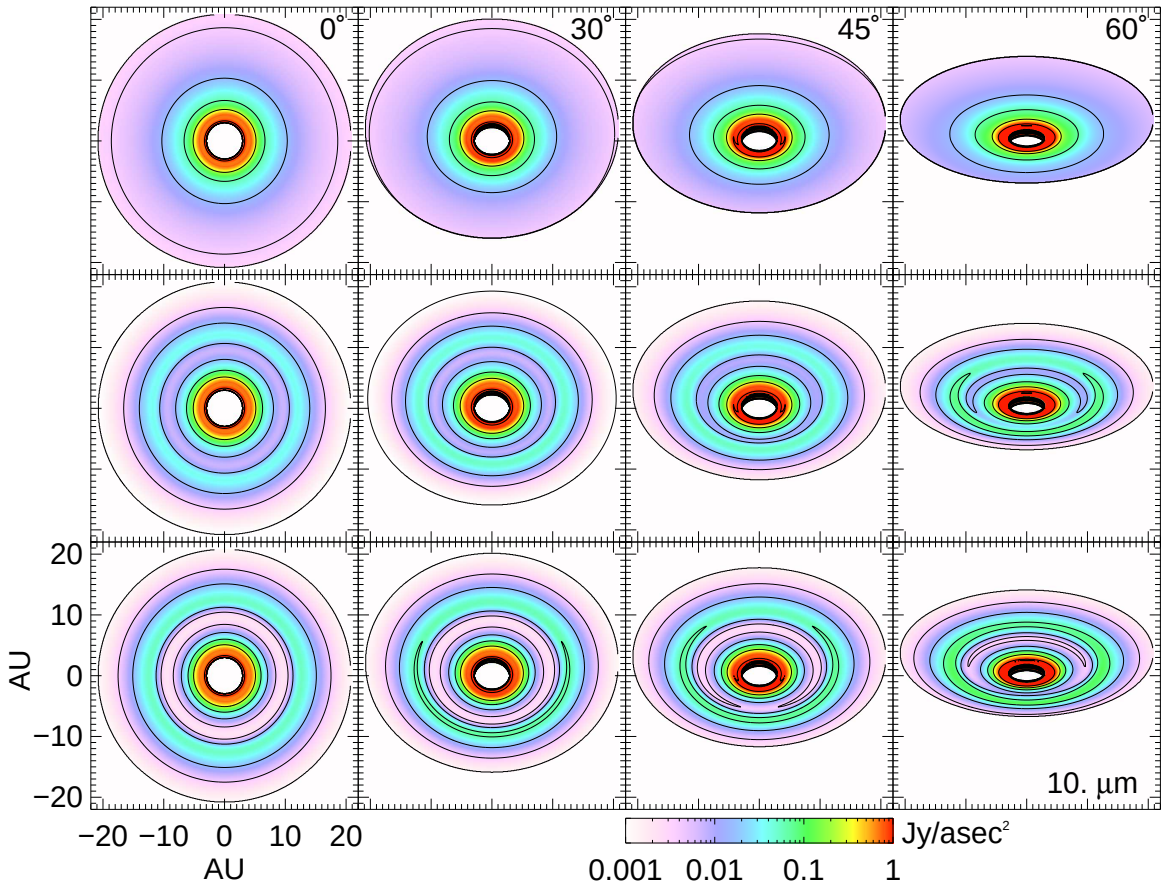

Figure 9. Same as Figure 8, at 10 μm. Contours are spaced by a factor of 4 in brightness.

this model to derive the inclination angle and thickness of a disk image. In order to reduce the number of free parameters, we make the assumption that $\partial z_s/\partial r \approx z_s/r$ or $\alpha \approx \beta$ and $\mu \approx 0$. We determine the best fits for i and β over 4 AU$< r_d <$20 AU by minimizing χ^2 between the brightness profile along the major axis and the harmonic mean of the brightness profiles along the near and far minor axes, using the MPFIT package (Markwardt 2009).[1] In this way, we are effectively measuring i and β from anisotropies in disk images.

The results of this fitting procedure are tabulated in the last two columns of Table 3. The fitting was done with no presumption about which side of the disk was near or far, but the correct orientation was still found. At all wavelengths and inclinations, the measured inclination angles are within 1°of the actual inclination. The measured values of z_s/r are reasonably accurate for scattered light, but less so for thermal wavelengths. This is in part because Equations (14)–(19) were derived from the equations for scattered light images. For example, the assumption that the imaging surface is independent of viewing angle is a reasonably good approximation for scattered light, since the illuminated layer of the disk is independent of viewing angle. However, at thermal wavelengths, the height of the imaging surface does depend on viewing angle, so that unless the transition from optically thin to thick is narrow, Equations (14)–(15) do not obtain. Nevertheless, we find that we can successfully recover the inclination angle of the disk, even if we cannot measure the aspect ratio of the disk (z_s/r) well.

Using Equations (14)–(19) to fit for i and z_s/r only works well if z_s/r varies slowly with r. Otherwise fitting to a a single value of α is inaccurate. Another effect that was not considered for these models was forward-scattering of light by small dust grains. A prediction of Mie theory is that small dust grains can be strongly forward-scattering, but scattering is assumed to be completely isotropic in the models presented here. On the other hand, if the anisotropy of the scattering can be well-described by a single parameter, such as in the Henyey-Greenstein model (Henyey & Greenstein 1941), the anisotropy may be treated as an additional fitting parameter and solved for accordingly. However, this is outside the scope of this paper.

3.2.2. *Inclined Disks: With Gaps*

Simulated images of inclined disks with gaps imposed on them by 70 and 200 $M_\oplus$ planets at 10 AU from the star are shown in the bottom two rows of Figures 8−13. As also seen in Varnière et al. (2006), the far shoulder of the gap is brightened in scattered light (Figure 8) regardless of inclination angle.

In the images of tilted gapped disks, the asymmetry in brightness between the near and far sides of the disk is more apparent than in the gapless disk. From 1 to 30 microns, the brightened shoulder of gap is brighter on the lower half of the disk, the side that is tipped toward the observer. In addition, the width of the shadow

[1] http://purl.com/net/mpfit

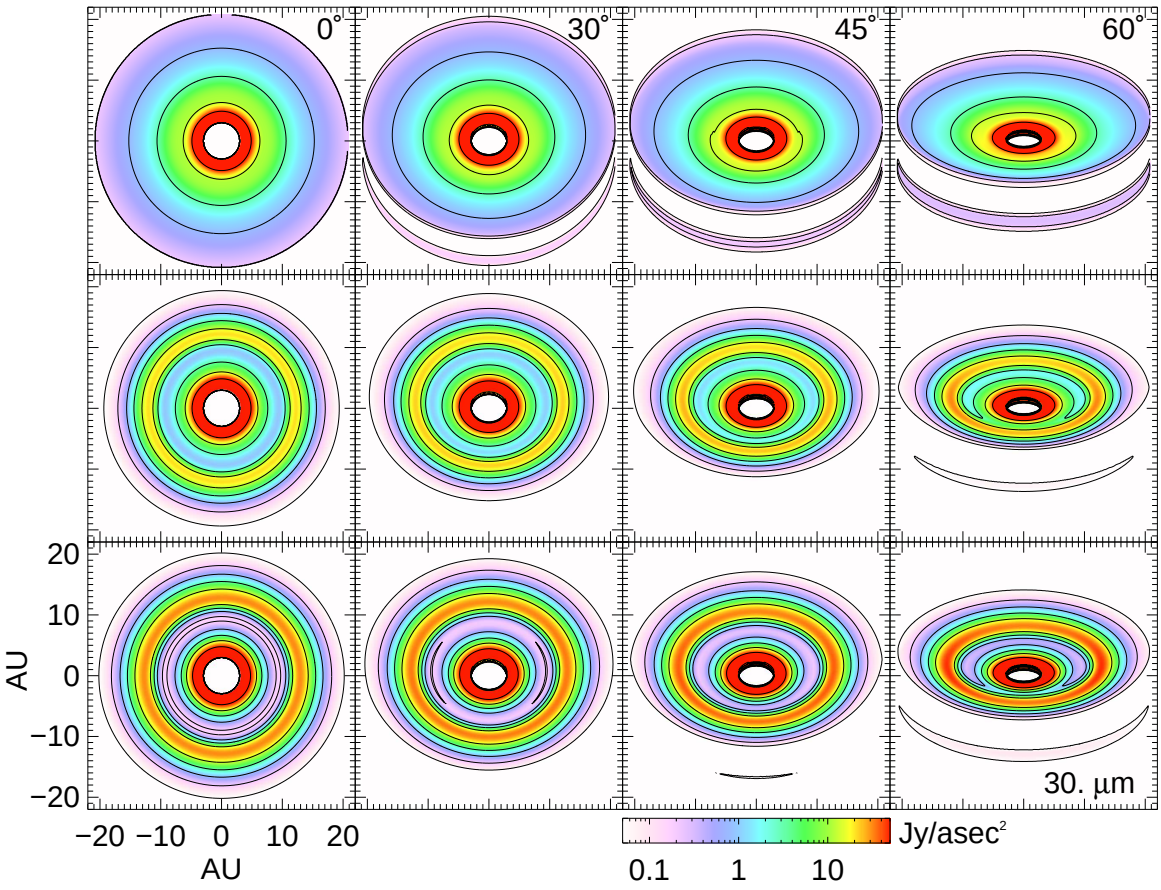

Figure 10. Same as Figure 8, at 30 μm. Contours are spaced by a factor of 4 in brightness.

within the gap is narrower on the near side because of the geometric foreshortening of the disk. At 100 microns and beyond, these asymmetries become less apparent as the disk becomes optically thin.

We can again make use of Eqs. (16-18) to estimate the brightness of the shadow in the gap and the brightened far shoulder as a function of PA. The gap in the disk makes the determination of disk thickness and inclination angle easier, because the shadow and brightening in the gap are points of reference that we can use to compare the profiles along different PA to each other.

Along the major axis, near minor axis, and far minor axis, we measure the surface brightness profile at each wavelength of observation as a function of projected radius. For each of these surface brightness profiles, we find the local minimum in brightness caused by the gap, and the local maximum on the far gap shoulder, labeling these points $r_{\rm min}$ and $r_{\rm max}$, respectively. We plot the flux ratio at these points versus $r_{\rm min}$ and $r_{\rm max}$ in Figure 15, where the flux ratio is defined to be the brightness at an extremum scaled to the disk brightness at 10 AU on the gap-less disk seen face-on. Variation of brightness extrema with wavelength, projection axis, planet mass, and inclination are indicated by the color, shape, size, and aspect ratio of symbols, respectively.

Before discussing the derived values of i and β from measurements of $r_{\rm max}$ and $r_{\rm min}$, we shall examine the variation of $r_{\rm max}$ and $r_{\rm min}$ and the brightnesses at these points as a function of wavelength, planet mass, and inclination angle. Each circle in Figure 15 represents the radius and flux ratio of the brightness extrema in a face-on disk for each of the two modeled planet masses as observed at a specific wavelength. The three branches coming off each circle indicate how the position and brightness of the extrema vary with along the major and minor axes as the inclination angles changes. Along the minor axis, $r_{\rm max}$ and $r_{\rm min}$ are scaled by $1/\cos i$ to partially account for inclination angle.

In nearly all cases, $r_{\rm max}/\cos i$ and $r_{\rm min}/\cos i$ is smaller on the near side than on the far side, with the values along the major axis somewhere in between. This is illustrated by the far side branches (marked by triangles, $\triangle$) lying to the right of the major axis branches ($+$), and near side branches ($\triangledown$) lying to the left in Figure 15. This is because the imaging surface is well above the midplane, creating additional foreshortening of the disk on the near side, and less on the far side of the disk. The few exceptions to these general trends occur at the longest wavelengths, 0.3 and 1 mm.

Additionally, $r_{\rm max}$ and $r_{\rm min}$ is smaller along the major axis of an inclined disk as compared to the $i = 0$ image in almost all cases. This is also due to the thickness of the disk. If one were to consider the ellipse traced by brightness maxima and minima along all azimuthal angles, the center of this ellipse would be offset from the position of the star, toward the direction of the far side. Because of this, a cut through the image through the star parallel to the major axis would be offset from the major axis of the ellipse, thus $r_{\rm max}$ and $r_{\rm min}$ as measured for Figure 15 are smaller along the major axis as compared

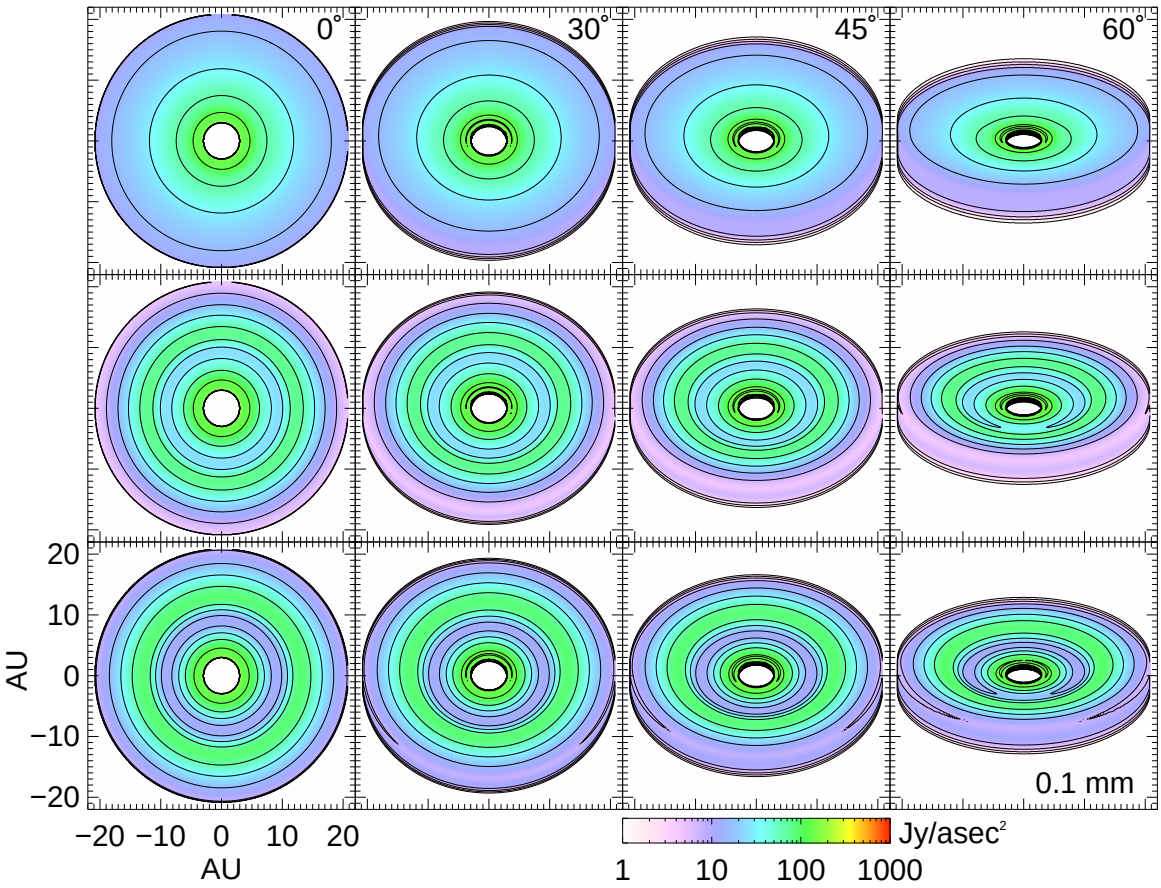

Figure 11. Same as Figure 8, at 0.1 mm. Contours are spaced by a factor of 2 in brightness.

to a face-on image.

The flux ratios of brightness minima have a larger spread than the brightness maxima, particularly for $\lambda \leq$ 0.1 mm. This is because tilting of the disk obstructs the shadowed region, decreasing the amount of contrast, particularly on the near side of the disk. At longer wavelengths, the disk becomes optically thin, and geometric brightening is no longer important.

The brightnesses along the major axis for $\lambda \lesssim 100$ μm are generally higher than for the face-on disk, increasing with i, because $\cos\eta = \cos\alpha \cos i$ (see Appendix A). That is, in scattered light, the viewing angle increases with increasing inclination angle, causing the disk to appear brighter. At longer wavelengths, on the other hand, we expect some dilution of brightness extrema as our line of sight through the disk changes, though the effect is small because of the decreasing opacity of the disk toward long wavelength. Hence, the brightness maxima become dimmer, and the brightness minima become brighter for $\lambda \gtrsim 0.3$ mm. Although images at 30 and 100 μmare of thermal emission, that emission comes from closer to the surface of the disk than at 0.3 or 1 mm, so there is less dilution of brightness along the line of sight, and the behavior with inclination angle is shares similarities to that for scattered light. The exception to these patterns are the brightness minima at $0.1 - 1$ mm (see inset of Figure 15). In some cases, the brightness minima along the major are dimmer as inclination increases, most notably for the 70 $M_\oplus$ planet observed at 0.3 mm. This is caused by the overall dimming of the disk with increasing inclination angle, also seen in Figure 14.

We find that the near side of the disk is systematically brighter than the far side at $r_{\rm min}$ and $r_{\rm max}$ than along the major axis for $\lambda \leq 30$ μm, as expected because η is larger on the near side than on the far side.

As in §3.2.1, we can use the geometric relations between r_d, r_n, and r_f to back out the inclination and aspect angles of the disk. From Eqs. (14-15),

$$\frac{1}{2}(r_f + r_n) = r_d \cos i \quad \text{and} \tag{20}$$

$$\frac{1}{2}(r_f - r_n) = r_d \sin i \tan\beta. \tag{21}$$

Using the measured values of $r_{\rm min}$ and $r_{\rm max}$ along the near and far minor axes as references point, we can then solve for the inclination (i) and aspect ratio ($z_s/r = \tan\beta$) of the disk from Eqs. (20-21). These derived values from simulated disk images are plotted in Figure 16.

For reference, values of i and z_s/r as calculated from full radial profiles of the fiducial disk model and tabulated in Table 3 are also plotted in Figure 16. Comparing these values to those plotted in Figure 16, we find that although it may be easier to calculate i and z_s/r by using the brightness maxima and minima as reference points, the values returned are not necessarily more accurate than those obtained by comparing the overall surface brightness profiles. Better accuracy can be obtained by averaging the values of i calculated from $r_{\rm max}$ and $r_{\rm min}$, although estimates of i are less accurate for the larger planet mass.

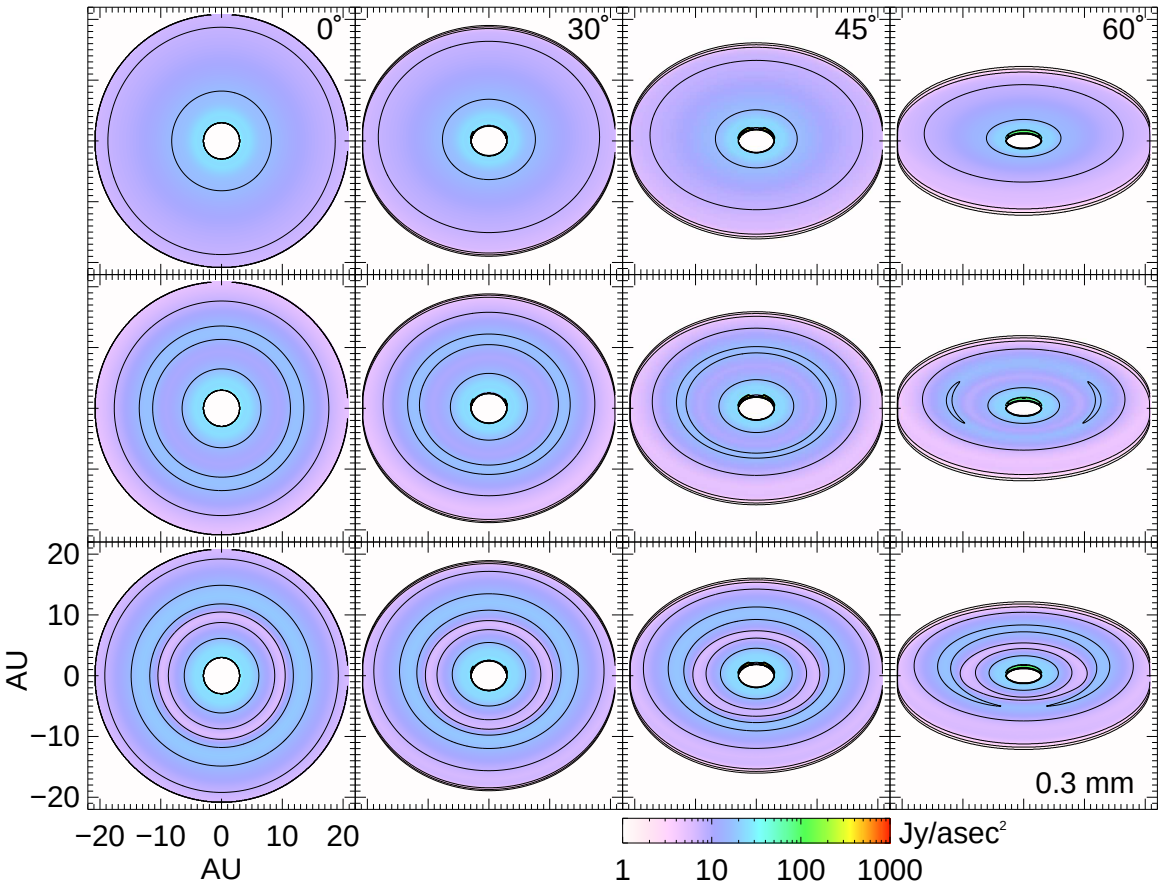

Figure 12. Same as Figure 8, at 0.3 mm. Contours are spaced by a factor of 2 in brightness.

Estimates of the aspect ratio of the disk are reasonably accurate in scattered light (1 and 10 μm), as seen in the lower panel of Figure 16. However, at thermal wavelengths ($\lambda \geq 30\,\mu$m), measurements of z_s/r from either radial profiles of gapless disks or brightness extrema in disks with gaps are less accurate in general. Both the measured and true values of z_s/r decrease with increasing wavelength, but the relation is steeper for the measured values. Thus, measurements at 30 μm all over-estimate z_s/r, while measurements at 1 mm all under-estimate z_s/r. Interestingly, the measured values are fairly consistent with each other across inclination angle, although there is a trend toward higher measured values of z_s/r with increasing inclination. This suggests that using a $\tau = 2/3$ height for the disk is not what is being probed by thermal emission. For example, at 30 μm, we are likely seeing emission from the hotter surface layer of the disk rather than to a $\tau = 2/3$ depth. Since this layer is higher above the midplane than the $\tau = 2/3$ depth, the measured aspect ratio is higher. At longer wavelengths, a likely explanation for the mismatch in aspect ratio is that thermal emission comes from broadly throughout the disk, as opposed to a vertically confined layer as in scattered light.

Finally, we note that our results hold only for circular gaps centered on the star. If the gap is eccentric, as might be produced by an eccentric planet, additional errors in the fitting will be introduced, and it will be difficult to disentangle changes in morphology produced from eccentricity versus inclination angle and disk thickness.

4. LKCA 15

To demonstrate the application of the simulated gapped disk images to real observations, we examine the case of LkCa 15. LkCa 15 is a T Tauri star that has been identified as having a transitional disk because it appears to have an inner cavity of radius 46 AU as inferred from its SED (Espaillat et al. 2007). The inner cavity has also been directly imaged by radio interferometry (Andrews et al. 2011b,a; Piétu et al. 2006; Isella et al. 2009), and in scattered light (Thalmann et al. 2010). LkCa 15 is also sometimes referred to as a "pre-transitional" disk because the inner cavity is not completely cleared (Espaillat et al. 2008).

One enticing possibility for the clearing of the inner disk in LkCa 15 is planet formation. Pott et al. (2010) observed no stellar companion down to 3.5 AU separations from the star. Recently, a possible planet has been imaged in its central cavity, at a deprojected distance of $\sim$ 20 AU (Kraus & Ireland 2012), but it is too far from the wall at 46 AU to be solely responsible for the inner clearing. Bonavita et al. (2010) put an upper limit of 5 $M_{\rm Jup}$ on a possible companion using NACO observations. From a theoretical standpoint, planets more massive than 6 $M_{\rm Jup}$ should cut off any accretion onto the star (Lubow et al. 1999), but Espaillat et al. (2007) find that the disk is still accreting onto the star at a rate of $\dot{M} = 2.4 \times 10^{-9}\,M_\odot\,{\rm yr}^{-1}$. Gas has been detected inside the cavity in the form of CO lines (Piétu et al. 2007), indicating an incompletely cleared inner disk. LkCa 15 also boasts a warm dust component at 0.12-0.15 AU as

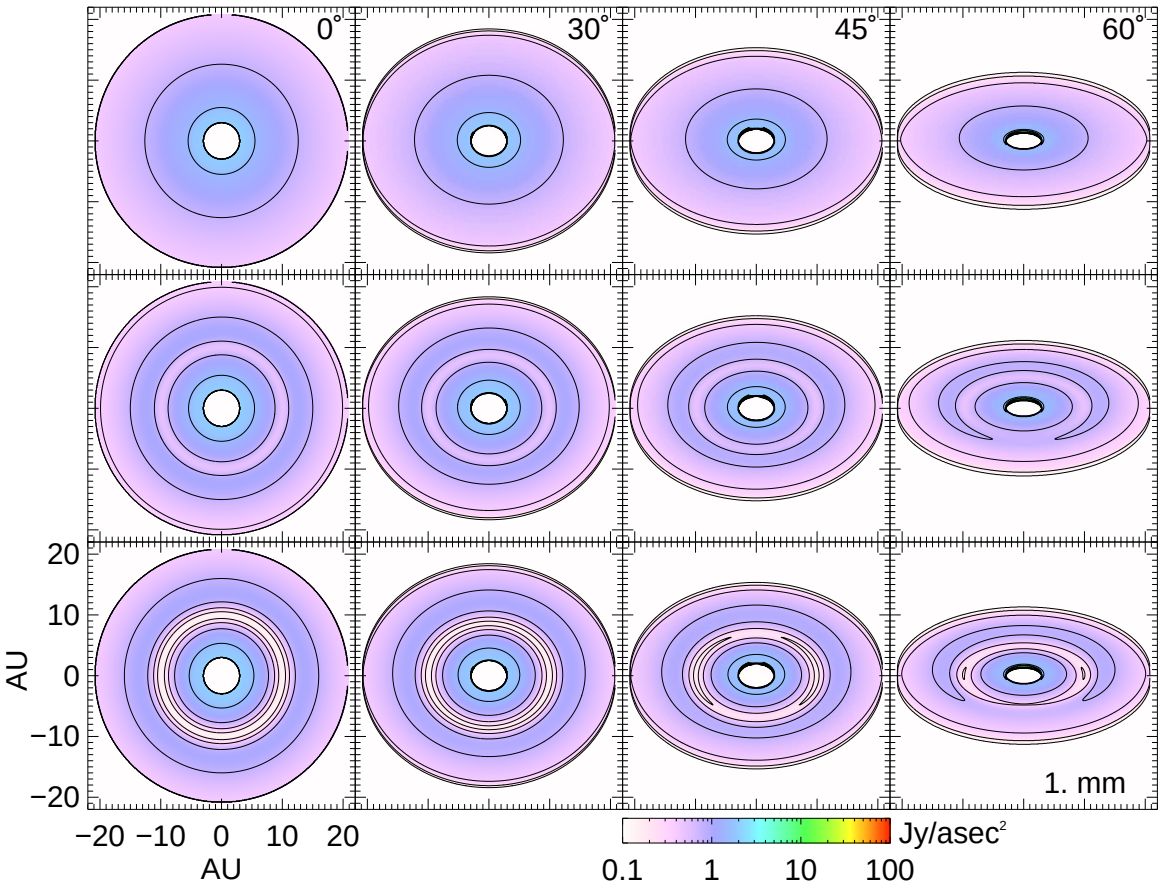

Figure 13. Same as Figure 8, at 1 mm. Contours are spaced by a factor of 2 in brightness.

inferred from its near-infrared excess (Espaillat et al. 2008), further evidence that the inner cavity is not completely cleared. All these lines of evidence point to the suggestion that one or more planetary-mass companions are responsible for the inner cavity in LkCa 15, with an upper limit on a single planet of 5 $M_{\rm Jup}$.

Using the methods outlined above, we can compare simulated images of gaps in disks created by planets of varying mass to the scattered light image of LkCa 15. Supposing that a single embedded planet is responsible for the inner clearing in LkCa 15, we can then put a constraint on the mass of a possible planet in LkCa 15. Although the models presented in this paper obtain for a radially contrained gap in a disk rather than a full inner clearing of all the material interior to a given radius within a disk, comparing the masses of planets capable of creating only gaps or partial gaps gives a useful lower bound on the mass of a possible planetary companion to LkCa 15.

LkCa 15 has a stellar mass of $M_* = 0.97 \pm 0.03\,M_\odot$, effective temperature $T_{\rm eff} = 4350$ K, and luminosity $L_* = 0.74\,L_\odot$ (Simon et al. 2000). Its disk is inclined at approximately 52°(Piétu et al. 2007) and its properties are well-fit with an accretion rate of $\dot{M} = 2.4 \times 10^{-9}\,M_\odot {\rm yr}^{-1}$ and $\alpha_{\rm ss} = 0.0007$ (Espaillat et al. 2007; Thalmann et al. 2010). For the purposes of this study, we round the stellar mass to $1\,M_\odot$ and derive a stellar radius of $R_* = 1.5\,R_\odot$ from the effective temperature and luminosity. These parameters are also listed in Table 1. We calculate a new disk model using the same procedures as for the fiducial model described above, but changing the parameters for the star and disk as constrained by observations. To simplify the calculation, the initial surface density profile is simply interpolated from a locally-plane parallel disk model rather than recalculating the full structure in detail. The radial range of this slice is from 9.5 to 99.5 AU, and the vertical range is 0 to 28.9 AU.

Since the width of a gap created by a planet varies with planet mass, a larger planet would be located further from the gap wall than a smaller planet. Thus, for a given gap size, we position it so that its half depth on the far side is at 46 AU. That is, we position the gap so that

$$\frac{\Sigma(r = 46\ {\rm AU})}{\Sigma_0(r = 46\ {\rm AU})} = 1/2 \qquad (22)$$

(where Σ without a subscript is the density profile with a gap and Σ_0 is the unperturbed density) with the gap trough interior to this distance. As in Paper I, we define the gap-opening threshold to be when $G = 1$, where G is the gap-opening parameter defined in Eq. 7. A planet with $G = 1$ opens a gap that is not well-modeled with Equation (22). Bate et al. (2003) calculate the surface density profile of a $1 M_J$ planet with $G = 1.04$ in their hydrodynamic simulations, and we adopt this as an axisymmetric gap profile without fitting to a Gaussian. The calculated gap parameters are summarized in Table 1 and their surface density profiles are plotted in Figure 17.

In Figure 18, we show observed and simulated H-band

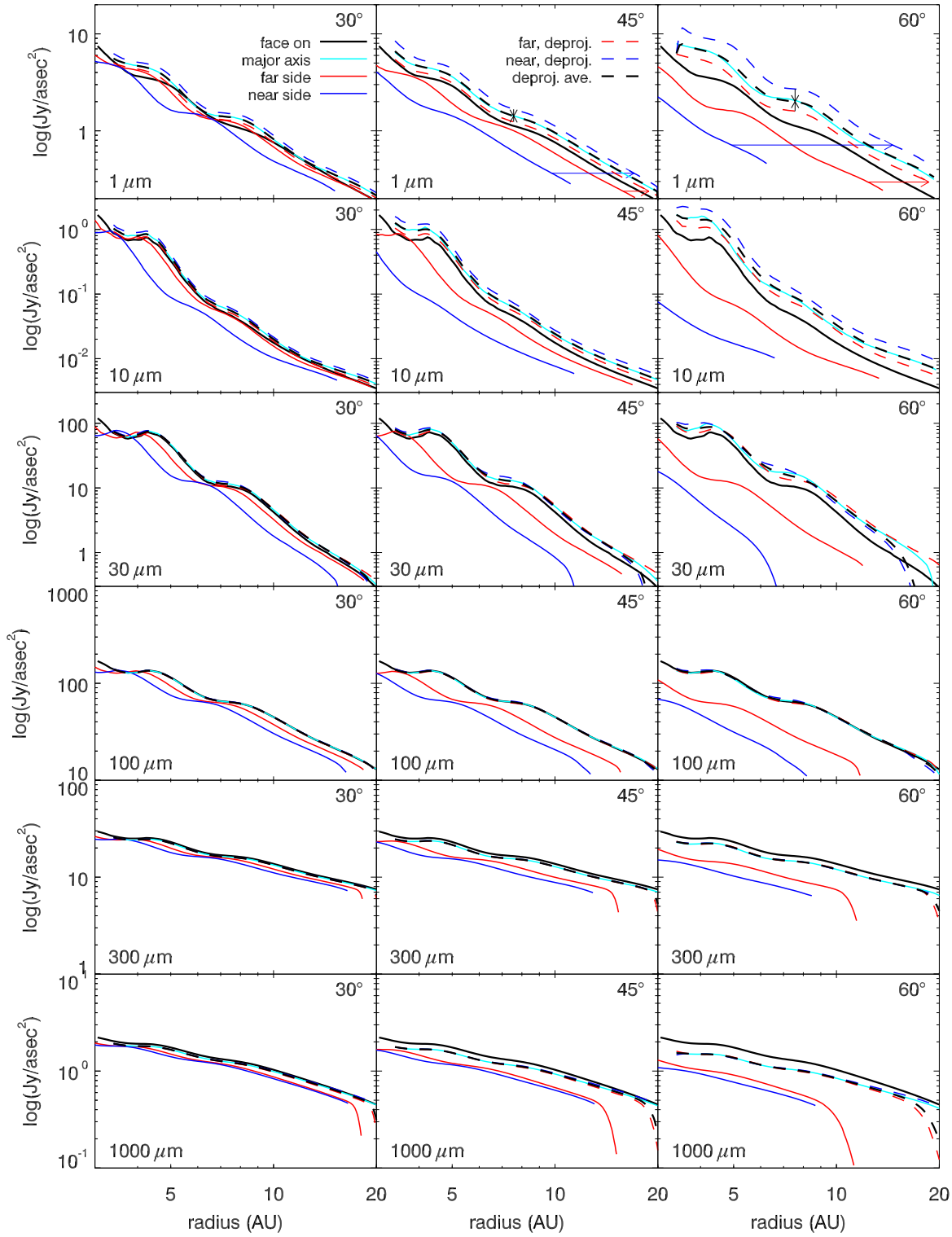

Figure 14. Radial surface brightness profiles of a disk without any gap at 1, 10, 30, 100, 300, and 1000 microns, as indicated. The solid black line is the profile for a face on disk. The cyan, red, and blue lines show the profiles for a disk tilted at 45°, along the major axis, far minor axis, and near minor axis, respectively. When the profiles along the minor axes are deprojected, accounting for both the inclination angle and the wavelength-dependent aspect angle, they shift to the red and blue dashed lines, respectively. The geometrical average of these deprojected curves is plotted as the black dashed line. At all wavelengths, this average deprojected profile is a good fit to the major axis. This relation may be an effective way to determine inclination angles of imaged protoplanetary disks.

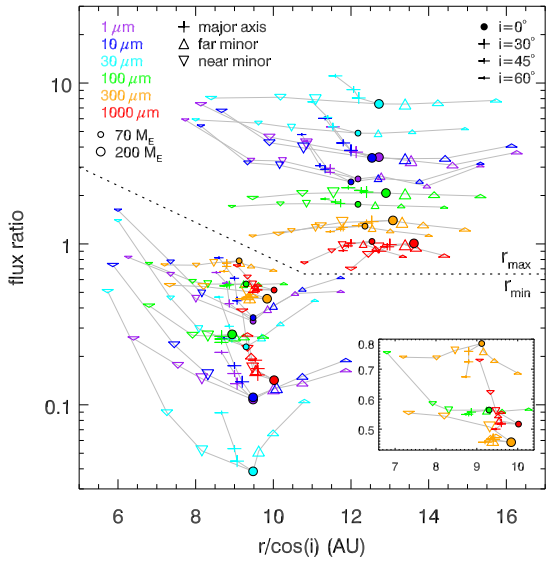

Figure 15. Flux ratios versus positions of brightness maxima and minima for disks with gaps at 10 AU, observed at varying inclination angle. The flux ratio is the brightness maximum or minimum divided by the brightness of a gapless disk at a radius of 10 AU from the star when observed at $i = 0°$. Brightness maxima/minima are plotted above/below the dotted line, and are measured along a cut through the disk image going through the star and parallel to either the major (+) or minor ($\triangle/\triangledown$ for far/near side) axis. Circles indicate disks with $i = 0°$, and the aspect ratio of the symbol decreases with increasing inclination angle. Gray lines connect model images varying with inclination angle. Along the minor axis, the radius is scaled by $1/\cos i$. The wavelength of observation is indicated by color: purple (1 μm), blue (10 μm), cyan (30 μm), green (0.1 mm), orange (0.3 mm), and red (1 mm). Smaller/larger points are used for gaps opened by 70/200 $M_\oplus$ planets. The inset clarifies the region of 6.5 AU $< r_{\rm min} <$ 10.5 AU.

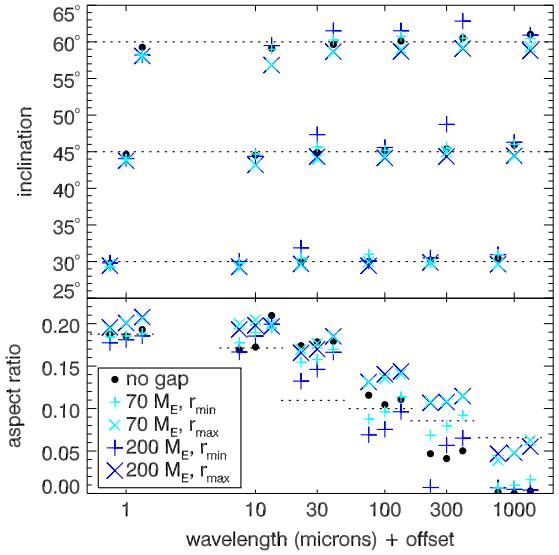

Figure 16. Inclination angles (top panel) and aspect ratios (bottom panel) calculated from simulated disk images as compared to actual values. The aspect ratio here is defined as $z_s/r = \tan\beta$. The horizontal axis is the wavelength of observation plus an offset corresponding to inclination angle, so that points from left to right have $i = 30°, 45°$, and $60°$. Actual values are indicated by horizontal dotted lines. Black circles indicate values tabulated in Table 3 for disks without gaps. Crosses (×) and plus symbols (+) indicate values derived from $r_{\rm max}$ and $r_{\rm min}$ measurements, respectively. Smaller cyan symbols indicate a disk model with a 70 $M_\oplus$ planet, while larger blue symbols indicate a model with 200 $M_\oplus$.

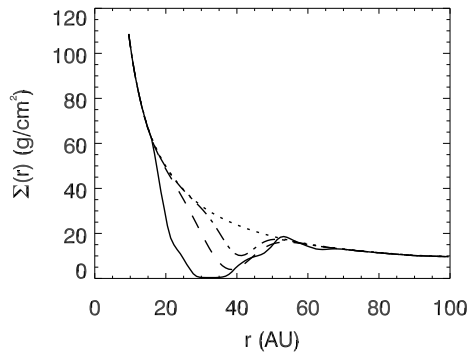

Figure 17. Surface density profiles of the disks used to model LkCa 15. The dotted line shows the unperturbed profile with no planet. The dot-dashed, dashed, and solid lines show gaps created by planets of 11, 37, and 154 $M_\oplus$ at 40.7, 38.3, and 32.5 AU, respectively.

images of LkCa 15. The upper left panel is the H-band Subaru image obtained by Thalmann et al. (2010), and the remaining panels are simulated images of our LkCa15 disk model with an 11 $M_\oplus$, 37 $M_\oplus$, and 0.5 M_J planet. The model disks are oriented so that the top part of the disk is the far edge, and the near edge is at the bottom. The center column of images are the fully resolved disk images, while the right column shows the images convolved with a Gaussian PSF of 0.55″, consistent with the resolution of the Thalmann, et al. image. The lower left image is the MC prediction for the 0.5 M_J planet case, using 10^8 photon packets. The morphology of the MC image is nearly identical to the JC image at bottom center of Figure 18. However, as discussed earlier, the gap shadow contrast is less in the MC image. All models over-predict thermal emission from the inner disk in the SED, indicating that the extent of disk clearing is wider than a gap created by a single planet of 0.5 M_J.

The brightness anisotropy in the model images is solely due to geometric effects. The point of maximum brightness is on the near side of the disk, but since the near side has a smaller angular size, when it is convolved with a realistic telescope resolution, the far side appears brighter overall. Thus, the model prediction is that the bright disk emission seen in the H-band image obtained by Thalmann et al. (2010, see top left panel of Figure 18) is from back-scattering off the inner wall of the outer disk.

The blacked-out inner circle in the simulated images in the right column of Figure 18 represents the 0″.055 FWHM PSF as reported in Thalmann et al. (2010). It is difficult to determine which model image (37 $M_\oplus$ or 0.5 M_J) is a better match to the observation, because they differ primarily in brightness, and the method used by Thalmann et al. to gain high contrast in order to image the disk does not preserve total flux. However, both models over-predict emission from the inner disk compared to the observational evidence. In our simulated images, the inner disk is quite bright and extends past the PSF circle, but this is not seen in the Thalmann et al. observation. Moreover, detailed analysis of LkCa 15's spectrum indicates that the dust in the inner disk extends no further than 5 AU (Espaillat et al. 2008). This suggests that either the gap in LkCa 15 is caused by a single planet more massive than 0.5 M_J, or there are

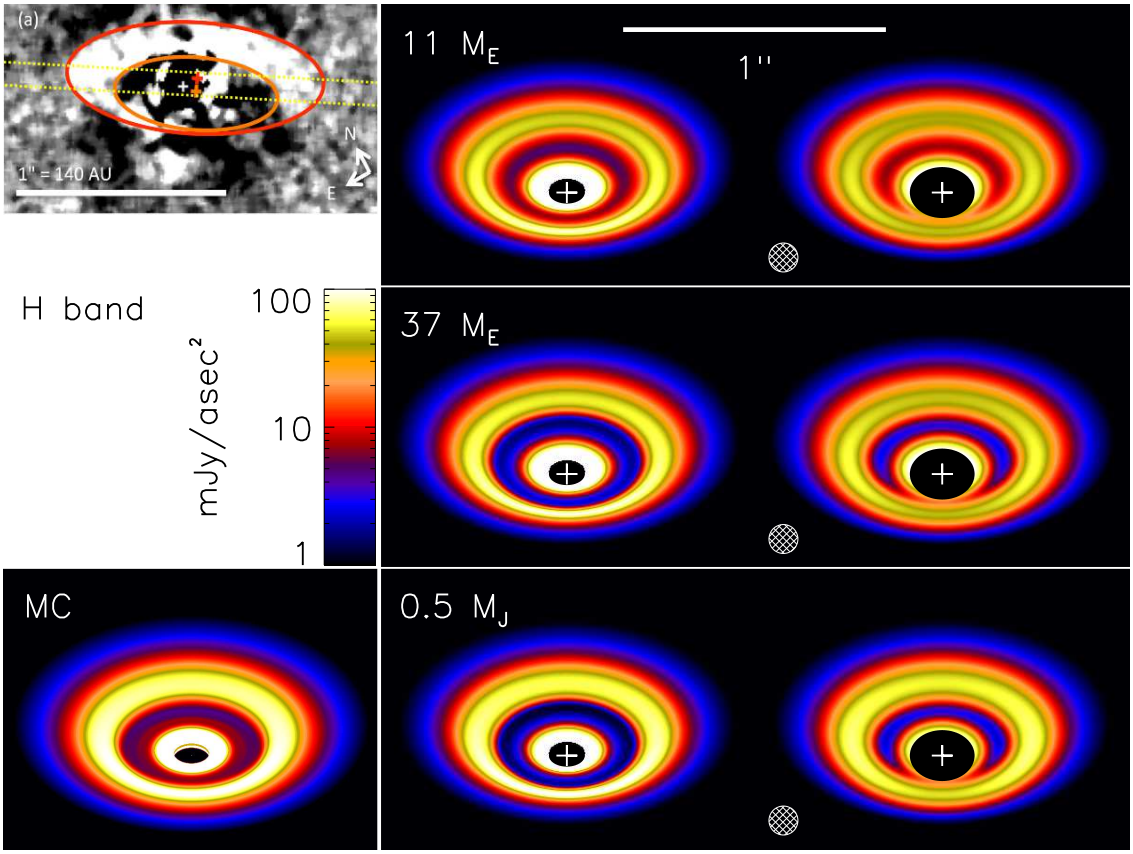

Figure 18. Observed and synthetic H-band images of the disk around LkCa 15. Upper left: H band image by Thalmann et al. (2010), with the scale bar representing 140 AU. Remaining images are synthetic images based on models for LkCa 15. The disk is inclined at 52°and oriented so that the top edge of the disk is tipped away from the observer. The white cross indicates the position of the central star, and the blacked out inner region is outside the simulation boundaries. The gaps in the models are created by 11 (top row), 37 (middle row), and 150 (bottom row) $M_\oplus$ planets. The images in the center column are the idealized JC models, while the images on the right have been convolved with a Gaussian PSF of FWHM of $0''.055$, as represented by the size of the hashed white circles. The lower left image is the MC image of the 150 $M_\oplus$ model, generated using 10^8 photon packets.

multiple planets in the gap.

Using the red and orange ellipses drawn on the top left panel of Figure 18, we can attempt to use the relations given in Eq. (20)-(21), using the midpoints between the two ellipses. Then, r_f, r_n and r_d are 28, 18, and 55 AU, respectively. This gives an inclination of 65°and $z_s/r = 0.1$. For comparison, our model has an assumed inclination of 52°, and $z_s/r = 0.2$ at 46 AU. However, the values measured from the observations are highly uncertain for two reasons: (1) the LOCI algorithm used for revealing the disk does not conserve flux so the measurements are highly uncertain themselves, and (2) the disk may be intrinsically elliptical, as evidenced by the offset of the star from the center of the major axis, in which case Eqs. (20)-(21) do not obtain, particularly Eq. (21), which depends on the difference between r_f and r_n, which is highly affected by a stellocentric offset.

In the center panel of Figure 19 we show the 0.5 M_J model for LkCa 15, this time imaged at 880 μm. The image has been convolved with a PSF matching that of Andrews et al. (2011b), i.e. with a beam size of $0.41'' \times 0.32''$ and rotated by $-3°$ with respect to the disk. We reproduce the flattening of the brightness profile in the inner region of the disk, as reported by Isella et al. (2009) and Piétu et al. (2006). However, we do not see the inner hole resolved by Andrews et al. (2011b) and reproduced in the left panel of Figure 19. When we simply remove the inner disk from the model and retain only the outer disk, as shown in the right panel of Figure 19, the morphology is very close to that of Andrews et al. (2011b). We reproduce the brightening of the far gap wall along the northwest minor axis, and the bright ansae along the major axis of the disk at the location of the gap wall. We even reproduce the brightness asymmetry along the southwest major axis, which results from the tilt of the elliptical PSF with respect to the major axis. This indicates that a gap in the disk is not a good model for LkCa 15, but rather a fully cleared inner hole, so if the clearing is caused by planet formation, the planet must be more than 0.5 M_J or there are multiple planets.

The planet candidate observed by Kraus & Ireland (2012) cannot have cleared all disk material out to the gap wall at 46 AU because it is too close to the star, but the observations do not rule out the presence of another planet. Multiple planets are capable of clearing out an inner hole enough so that it is optically thin, but still allows continued accretion onto the star (Dodson-Robinson & Salyk 2011). A definitive measurement of the position of an additional planet in LkCa 15 could be obtained by determining the orbital velocity of non-axisymmetric structure of the disk. A planet would be expected to raise spiral arms in the disk, whose pattern

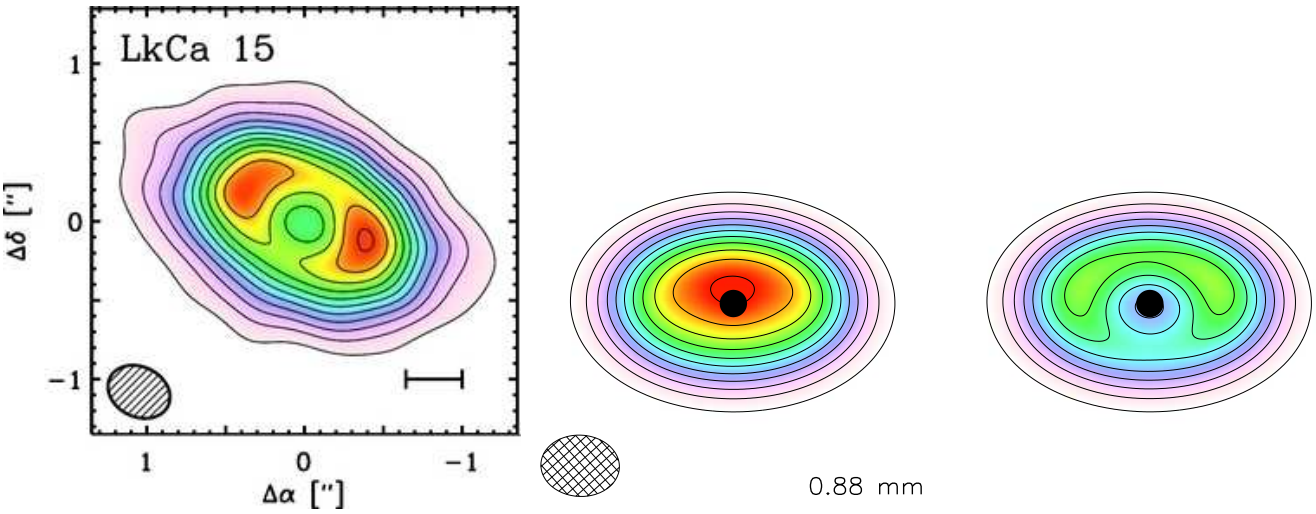

Figure 19. Observed and synthetic images of the disk around LkCa15 with at 880 μm. The left panel is the SMA image obtained by Andrews et al. (2011b), with the scale bar representing 50 AU, showing a deficit of disk material in the inner $\sim$ 50 AU of the disk. The center and right panels are synthetic images of the LkCa 15 disk modeled with a 0.5 M_J planet, convolved with a PSF $0.41'' \times 0.32''$ in size, rotated by -3° with respect to the disk major axis, matching the observations of LkCa 15 with the SMA (Andrews et al. 2011b) and indicated by the hashed ellipse. Contours are spaced at intervals of 30 mJy/asec^2 beginning at 30 mJy/asec^2. The center panel shows the image of the disk modeled with a radially confined gap, with the black filled circle centered on the star. The right panel shows the image of the same disk but with all emission from the inner disk removed. The morphology of the centrally cleared image is a better match to the observations, including the brightened ansae and far disk wall. The right ansa is slightly brighter than the left, purely as a result of the orientation of the PSF.

speed would be that of the planet, rather than the local Keplerian orbital speed. Thus, a planet with semi-major axis a would complete an orbit in $(a/1\ \mathrm{AU})^{3/2}$ years, so a feature on the inner wall of the disk at 46 AU should orbit at a rate of $2''\ \mathrm{yr}^{-1} \times (a/1\ \mathrm{AU})^{-3/2}$, or 11, 9, or 8 mas/yr for a planet at 33, 38, or 41 AU, respectively, with some variation due to the inclination of the disk.

We have shown that a gap created in a disk by a single planet does not successfully reproduced resolved images of LkCa 15, leading to the conclusion that the inner disk is mostly cleared out. In Figure 20, we show predicted radio images of the LkCa 15 disk model with a cleared inner hole, from the right panel for Figure 19. The images are continuum emission at 1.3, 0.88, and 0.45 mm, wavelengths that ALMA is able to probe. The images are convolved with PSFs of varying sizes to illustrate how the apparent morphology of the disk changes with different beam sizes. If the beam size is larger than the angular size of the brightened inner wall, the brightness of the feature will be diminished and diluted. These images demonstrate that ALMA should be able to clearly resolve the inner hole in LkCa 15, and determine just how empty the inner clearing is.

The inner hole model shown above is a lower limit on the brightness of the inner wall. The model is based on a disk model with a deep, wide gap, and then simply subtracting emission from the inner disk. The model was calculated assuming the presence of an inner disk, which would prevent full illumination of the inner wall of a cleared hole. In a disk with a true inner hole, the wall will be hotter and therefore brighter. The brightened wall exposed by the inner clearing may partially shadow the disk material behind it, creating still more contrast between the inner wall and the disk outside it.

5. DISCUSSION AND CONCLUSIONS

The gaps modeled in this paper are based on a simple parameterized structure for the gap. Real gaps created by planets in disks may show non-axisymmetric structure not captured in this simple model. Thus, while the models and simulated images presented in this work give a good qualitative description of the effects of gap-opening on disks, the magnitude of shadowing and illumination effects may vary depending on the exact disk properties.

Since the models presented here do not include hydrodynamics, the effects of accretion onto the embedded planet have been neglected. We can estimate the accretion rates from the empirical determination of Bate et al. (2003),

$$\dot{M}_p = b\frac{M_p}{M_*}\rho\Omega_p a^3 \tag{23}$$

where $b \approx 2.3$. For the 70 and 200 $M_\oplus$ planets modeled here, the estimated accretion rate is about $\sim 10^{-4}\, M_J\ \mathrm{yr}^{-1}$. We can estimate the accretion luminosity as

$$L_{\mathrm{acc}} = \frac{G_{gr} M_p \dot{M}_p}{r_{\mathrm{Hill}}} \tag{24}$$

where G_{gr} is the gravitational constant. The Hill radius is 0.4 and 0.6 AU for the 70 and 200 $M_\oplus$ planet, respectively. Then the accretion luminosity is 3×10^{28} and 6×10^{28} erg s^{-1}, respectively. Assuming that the material interior to the Hill sphere is optically thick, then the effective temperature may be expressed as $T_{\mathrm{eff}} = (L_{\mathrm{acc}}/(4\pi r_{\mathrm{Hill}}^2 \sigma_B))^{1/4}$. The resultant temperature is about $\sim$ 30 K for both planet masses, while the midplane temperature in the absence of this accretion heating is 46 K and 39 K for the 70 and 200 $M_\oplus$ planet, respectively. The additional heating may be expressed as $T = (T_1^4 + T_2^4)^{1/4}$, so the addition of the accretion luminosity would raise the temperature immediately around the planet by a few degrees. The modest amount of heating suggests that little to no detectable change in the structure of the disk would result. The amount of heating could be increased if the radius of accretion were less

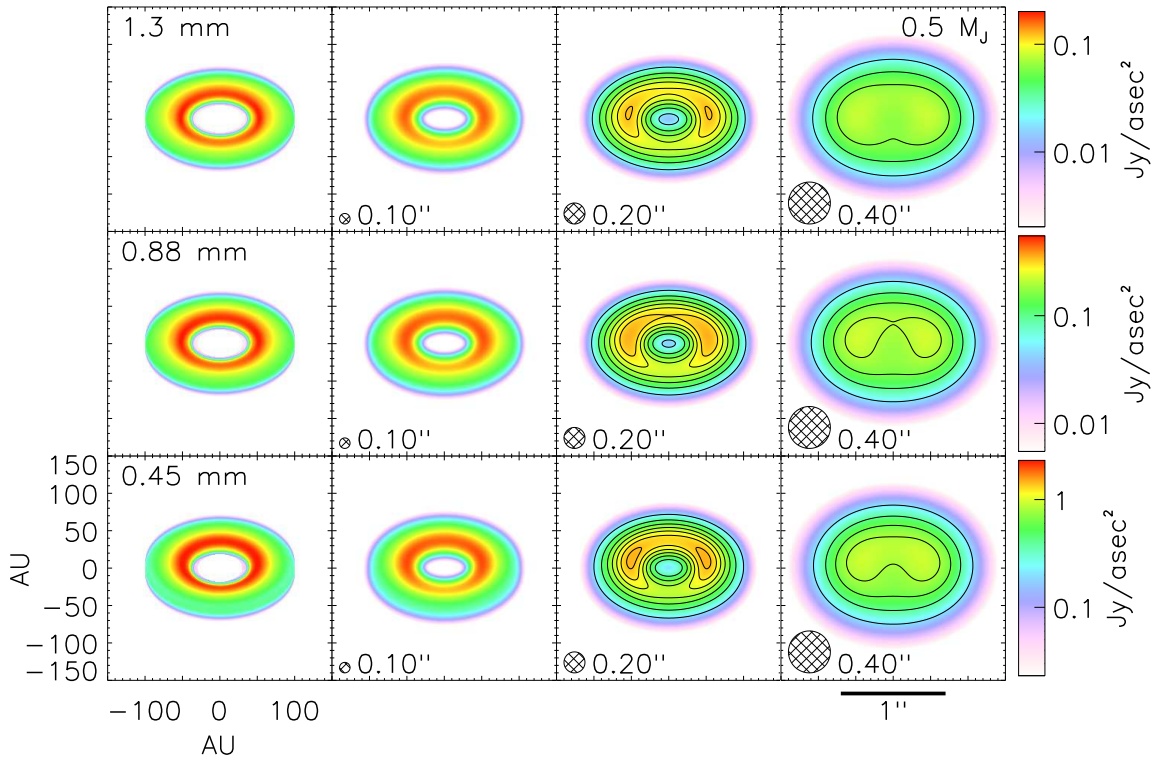

Figure 20. Simulated radio images of LkCa 15 with an inner hole in its disk at 1.3 mm (top), 0.88 mm (middle), and 0.45 mm (bottom). The leftmost column shows the original, fully resolved disk image. In the remaining columns, from left to right, the image has been convolved with a PSF of 0.1″, 0.2″, and 0.4″, respectively, as indicated by the circles in the lower left corner of each plot. Contours are spaced at intervals of 20, 50, and 200 mJy-asec^{-2} at 1.3, 0.88 and 0.45 mm, respectively. Contours are not shown in the left two columns for clarity. At these wavelengths, the far edge appears brighter at smaller angular resolution not because of an inherent difference in brightness, but because the angular size of the frontally illuminated far side of the gap is larger than the near side.

than the Hill radius, but that calculation is outside the scope of this paper. In any case, the heating from the planet would be a local asymmetric perturbation on the disk structure and the structure of the gap upstream and downstream of the planet would be unchanged.

We have shown that the geometric effects of inclined disks, with or without gaps, can create structure in disk images that must be interpreted carefully. The effect of inclination on disk images varies with wavelength, since scattered light images in the optical or infrared probe only the disk surface, while radio frequency images probe the deep thermal structure of the disk.

The scattered light models here (1 μm images) apply over a limited range of inclination angles, in that the brightness calculated is that scattered off the surface of the disk, rather than light seen extinguished through the disk. That is, our models do not apply to a system such as HH 30, which is nearly edge on (Cotera et al. 2001), so that the observed scattered light is seen through the disk.

Comparing brightness profiles along different axes can yield the inclination and aspect ratio of the disk, under the assumption of axisymmetry. This can be done, in principle, at any wavelength, whether in scattered light or thermal emission, and with or without a gap in the disk.

When a gap is opened in an inclined disk, the near side of the gap's outer wall appears slightly brighter than the far side at the point of maximum brightness. However, if the illuminated wall is unresolved in the observation, then the far side may appear brighter because it spans a larger angular size. A gap in a disk may aid in the calculation of inclination angle and aspect ratio of a disk, but only if the gap is not eccentric. An eccentric gap, possibly created by an embedded planet, affects the derivation of aspect ratio more than the inclination angle, as shown in the example of LkCa 15.

Our example of LkCa 15 demonstrates that gaps in disks are currently detectable in scattered light. However, the gap in LkCa15 is at a much larger radius (~ 50 AU) compared to the gap at 10 AU as modeled in the first part of this paper. Supposing that the 10 AU gap was in a disk at 140 pc, the distance of Taurus, would the gap be detectable? The gaps modeled were 1.1 and 1.7 AU in width, respectively, or 8 and 12 mas, respectively. Observing at 1 micron at the diffraction limit, this would require a $17-27$ m telescope to resolve. At 0.3 mm, the baseline required would be $5-8$ km. Large optical telescopes such as the LBT, GMT, and TMT, and the radio array ALMA would achieve such resolving power, but prospects for imaging gaps at mid- to far-infrared wavelengths are small. In the optical, high contrast imaging would also be necessary. An inner working angle of 0″.05 would block out the inner 7 AU of the disk. At sub-mm to mm wavelengths, stellar contrast is not an issue, but the contrast within the gap itself is much less than at shorter wavelengths. At 0.3 and 1 mm, the required sensitivity is on order of 1 and 0.1 Jy/asec^2, or 1.4 and 0.15

K respectively. In band 9 of ALMA (0.45 mm), the required integration time for 10 mas resolution with 1.4 K sensitivity using 50 antennas is 22 hours. At 1 mm (band 7), 0.15 K sensitivity requires 13 hours.

By comparing resolved images of disks to the models presented here, we can estimate the masses of planets that might be causing those gaps. In particular, we put a lower mass limit of 0.5 Jupiter masses on a planetary companion in LkCa 15 that would create the observed inner hole. If planets are responsible for the inner hole, then our results suggest that it is either caused by a more massive planet or by multiple planets with overlapping gaps.

The authors thank C. A. Grady and A. Hubbard for helpful discussions in the preparation of this paper. We also thank an anonymous referee for constructive comments that greatly improved this paper. H.J.-C. acknowledges support from the NASA Astrophysics Theory Program through grant NNX12AD43G and the the Michelson Fellowship Program under contract with the Jet Propulsion Laboratory (JPL) funded by NASA. N.J.T. was employed by JPL, which is managed for NASA by the California Institute of Technology. He was supported by the NASA Origins of Solar Systems program through grant 09-SSO09-0046, and by the Humboldt Foundation through a Fellowship for Experienced Researchers.

APPENDIX

SCATTERING ANGLES

In this Appendix, we show how to calculate η, the angle between the surface normal and the observer, assuming an axisymmetric disk. For a general surface, $z = f(x, y)$, the unit surface normal can be expressed as

$$\hat{\mathbf{n}} = \frac{-(\partial z/\partial x)\hat{\mathbf{x}} - (\partial z/\partial y)\hat{\mathbf{y}} + \hat{\mathbf{z}}}{\sqrt{(\partial z/\partial x)^2 + (\partial z/\partial y)^2 + 1}}$$

Without loss of generality, we place the disk midplane in the xy plane and the observer in the 1st quadrant of the xz plane. Then, if the inclination angle is i, the vector toward the observer is $\hat{\mathbf{m}} = \sin i\,\hat{\mathbf{x}} + \cos i\,\hat{\mathbf{z}}$. Then the cosine of the angle between the surface normal and observer is

$$\cos\eta = \hat{\mathbf{n}} \cdot \hat{\mathbf{m}} = \frac{-(\partial z/\partial x)\sin i + \cos i}{\sqrt{(\partial z/\partial x)^2 + (\partial z/\partial y)^2 + 1}}$$

We convert this to cylindrical coordinates, with

$$\begin{aligned} x &= r\cos\theta \\ y &= r\sin\theta \\ z &= z \end{aligned}$$

and using the chain rule to get

$$\begin{aligned} \frac{\partial z}{\partial x} &= \cos\theta\frac{\partial z}{\partial r} - \frac{\sin\theta}{r}\frac{\partial z}{\partial \theta} \\ \frac{\partial z}{\partial y} &= \sin\theta\frac{\partial z}{\partial r} + \frac{\cos\theta}{r}\frac{\partial z}{\partial \theta} \end{aligned} \tag{A1}$$

and find

$$\cos\eta = \frac{\cos i - [\cos\theta(\partial z/\partial r) + (\sin\theta/r)(\partial z/\partial\theta)]\sin i}{\sqrt{(\partial z/\partial r)^2 + (1/r^2)(\partial z/\partial\theta)^2 + 1}}. \tag{A2}$$

In an axisymmetric disk, $\partial z/\partial\theta = 0$. Defining $\tan\alpha = \partial z/\partial r$,

$$\cos\eta = \cos\alpha\cos i - \cos\theta\sin\alpha\sin i. \tag{A3}$$

Since the observer is located toward positive x, the far side of the disk is $\theta = \pi$ and the near side of the disk is $\theta = 0$. Hence, on the far side of the disk, $\eta_1 = i - \alpha$ and on the near side $\eta_2 = i + \alpha$. At maximum elongation, $\theta = \pm\pi/2$ and $\cos\eta = \cos\alpha\cos i$.

REFERENCES

Andrews, S. M., Rosenfeld, K. A., Wilner, D. J., & Bremer, M. 2011a, ApJ, 742, L5

Andrews, S. M., Wilner, D. J., Espaillat, C., Hughes, A. M., Dullemond, C. P., McClure, M. K., Qi, C., & Brown, J. M. 2011b, ApJ, 732, 42

Ayliffe, B. A. & Bate, M. R. 2009, MNRAS, 393, 49

Bate, M. R., Lubow, S. H., Ogilvie, G. I., & Miller, K. A. 2003, MNRAS, 341, 213

Biller, B., Lacour, S., Juhász, A., Benisty, M., Chauvin, G., Olofsson, J., Pott, J.-U., Müller, A., Sicilia-Aguilar, A., Bonnefoy, M., Tuthill, P., Thebault, P., Henning, T., & Crida, A. 2012, ApJ, 753, L38

Bonavita, M., Chauvin, G., Boccaletti, A., Pietu, V., Baudoz, P., Beuzit, J. L., Dutrey, A., Guilloteau, S., Lagrange, A. M., Mouillet, D., & Niccolini, G. 2010, ArXiv e-prints

Cieza, L. A., Mathews, G. S., Williams, J. P., Ménard, F. C., Kraus, A. L., Schreiber, M. R., Romero, G. A., Orellana, M., & Ireland, M. J. 2012, ApJ, 752, 75

Cotera, A. S., Whitney, B. A., Young, E., Wolff, M. J., Wood, K., Povich, M., Schneider, G., Rieke, M., & Thompson, R. 2001, ApJ, 556, 958
Crida, A., Morbidelli, A., & Masset, F. 2006, Icarus, 181, 587
de Val-Borro, M., Edgar, R. G., Artymowicz, P., Ciecielag, P., Cresswell, P., D'Angelo, G., Delgado-Donate, E. J., Dirksen, G., Fromang, S., Gawryszczak, A., Klahr, H., Kley, W., Lyra, W., Masset, F., Mellema, G., Nelson, R. P., Paardekooper, S., Peplinski, A., Pierens, A., Plewa, T., Rice, K., Schäfer, C., & Speith, R. 2006, MNRAS, 370, 529
Dodson-Robinson, S. E. & Salyk, C. 2011, ApJ, 738, 131
Dullemond, C. P. & Dominik, C. 2004, A&A, 417, 159
Edgar, R. G. & Quillen, A. C. 2008, MNRAS, 387, 387
Espaillat, C., Calvet, N., D'Alessio, P., Hernández, J., Qi, C., Hartmann, L., Furlan, E., & Watson, D. M. 2007, ApJ, 670, L135
Espaillat, C., Calvet, N., Luhman, K. L., Muzerolle, J., & D'Alessio, P. 2008, ApJ, 682, L125
Hashimoto, J., Dong, R., Kudo, T., Honda, M., McClure, M., Zhu, Z., Muto, T., Wisniewski, J., Abe, L., Brandner, W., Brandt, T., Carson, J., Egner, S., Feldt, M., Fukagawa, M., Goto, M., Grady, C. A., Guyon, O., Hayano, Y., Hayashi, M., Hayashi, S., Henning, T., Hodapp, K., Ishii, M., Iye, M., Janson, M., Kandori, R., Knapp, G., Kusakabe, N., Kuzuhara, M., Kwon, J., Matsuo, T., Mayama, S., McElwain, M., Miyama, S., Morino, J.-I., Moro-Martin, A., Nishimura, T., Pyo, T.-S., Serabyn, G., Suenaga, T., Suto, H., Suzuki, R., Takahashi, Y. H., Takami, M., Takato, N., Terada, H., Thalmann, C., Tomono, D., Turner, E. L., Watanabe, M., Yamada, T., Takami, H., Usuda, T., & Tamura, M. 2012, ArXiv e-prints
Henyey, L. G. & Greenstein, J. L. 1941, ApJ, 93, 70
Huélamo, N., Lacour, S., Tuthill, P., Ireland, M., Kraus, A., & Chauvin, G. 2011, A&A, 528, L7
Isella, A., Carpenter, J. M., & Sargent, A. I. 2009, ApJ, 701, 260
Jang-Condell, H. 2008, ApJ, 679, 797
—. 2009, ApJ, 700, 820
Jang-Condell, H. & Boss, A. P. 2007, ApJ, 659, L169
Jang-Condell, H. & Sasselov, D. D. 2003, ApJ, 593, 1116
—. 2004, ApJ, 608, 497
Jang-Condell, H. & Turner, N. J. 2012, ApJ, 749, 153
Kraus, A. L. & Ireland, M. J. 2012, ApJ, 745, 5
Lubow, S. H., Seibert, M., & Artymowicz, P. 1999, ApJ, 526, 1001
Markwardt, C. B. 2009, in Astronomical Society of the Pacific Conference Series, Vol. 411, Astronomical Data Analysis Software and Systems XVIII, ed. D. A. Bohlender, D. Durand, & P. Dowler, 251–+
Mathews, G. S., Williams, J. P., & Ménard, F. 2012, ApJ, 753, 59
Mulders, G. D., Dominik, C., & Min, M. 2010, A&A, 512, A11+
Paardekooper, S. & Papaloizou, J. C. B. 2008, A&A, 485, 877
Piétu, V., Dutrey, A., & Guilloteau, S. 2007, A&A, 467, 163
Piétu, V., Dutrey, A., Guilloteau, S., Chapillon, E., & Pety, J. 2006, A&A, 460, L43
Pinte, C., Padgett, D. L., Ménard, F., Stapelfeldt, K. R., Schneider, G., Olofsson, J., Panić, O., Augereau, J. C., Duchêne, G., Krist, J., Pontoppidan, K., Perrin, M. D., Grady, C. A., Kessler-Silacci, J., van Dishoeck, E. F., Lommen, D., Silverstone, M., Hines, D. C., Wolf, S., Blake, G. A., Henning, T., & Stecklum, B. 2008, A&A, 489, 633
Pott, J., Perrin, M. D., Furlan, E., Ghez, A. M., Herbst, T. M., & Metchev, S. 2010, ApJ, 710, 265
Ruge, J. P., Wolf, S., Uribe, A. L., & Klahr, H. H. 2013, A&A, 549, A97
Shakura, N. I. & Sunyaev, R. A. 1973, A&A, 24, 337
Siess, L., Dufour, E., & Forestini, M. 2000, A&A, 358, 593
Simon, M., Dutrey, A., & Guilloteau, S. 2000, ApJ, 545, 1034
Tannirkulam, A., Monnier, J. D., Harries, T. J., Millan-Gabet, R., Zhu, Z., Pedretti, E., Ireland, M., Tuthill, P., ten Brummelaar, T., McAlister, H., Farrington, C., Goldfinger, P. J., Sturmann, J., Sturmann, L., & Turner, N. 2008, ApJ, 689, 513
Thalmann, C., Grady, C. A., Goto, M., Wisniewski, J. P., Janson, M., Henning, T., Fukagawa, M., Honda, M., Mulders, G. D., Min, M., Moro-Martín, A., McElwain, M. W., Hodapp, K. W., Carson, J., Abe, L., Brandner, W., Egner, S., Feldt, M., Fukue, T., Golota, T., Guyon, O., Hashimoto, J., Hayano, Y., Hayashi, M., Hayashi, S., Ishii, M., Kandori, R., Knapp, G. R., Kudo, T., Kusakabe, N., Kuzuhara, M., Matsuo, T., Miyama, S., Morino, J., Nishimura, T., Pyo, T., Serabyn, E., Shibai, H., Suto, H., Suzuki, R., Takami, M., Takato, N., Terada, H., Tomono, D., Turner, E. L., Watanabe, M., Yamada, T., Takami, H., Usuda, T., & Tamura, M. 2010, ApJ, 718, L87
Turner, N. J., Choukroun, M., Castillo-Rogez, J., & Bryden, G. 2012, ApJ, 748, 92
Varnière, P., Bjorkman, J. E., Frank, A., Quillen, A. C., Carciofi, A. C., Whitney, B. A., & Wood, K. 2006, ApJ, 637, L125
Walker, C., Wood, K., Lada, C. J., Robitaille, T., Bjorkman, J. E., & Whitney, B. 2004, MNRAS, 351, 607
Wolf, S. & D'Angelo, G. 2005, ApJ, 619, 1114